



Article

Understanding Complex Interplay among Different Instabilities in Multiferroic $\text{BiMn}_7\text{O}_{12}$ Using ^{57}Fe Probe Mössbauer Spectroscopy

Iana S. Soboleva ¹, Vladimir I. Nitsenko ¹, Alexey V. Sobolev ^{1,2,*}, Maria N. Smirnova ^{1,3}, Alexei A. Belik ⁴ and Igor A. Presniakov ^{1,2}

¹ Department of Chemistry, Lomonosov Moscow State University, Moscow 119991, Russia; janglaz@bk.ru (I.S.S.); nvova.chem@gmail.com (V.I.N.); ipresniakov1969@mail.ru (I.A.P.)

² Department of Chemistry, MSU-BIT University, Shenzhen 517182, China

³ Kurnakov Institute of General and Inorganic Chemistry of Russian Academy of Sciences (RAS), Moscow 119991, Russia

⁴ Research Center for Materials Nanoarchitectonics (MANA), National Institute for Materials Science (NIMS), Namiki 1-1, Tsukuba 305-0044, Ibaraki, Japan; alexei.belik@nims.go.jp

* Correspondence: alex@radio.chem.msu.ru

Abstract: Here, we report the results of a Mössbauer study on hyperfine electrical and magnetic interactions in quadruple perovskite $\text{BiMn}_7\text{O}_{12}$ doped with ^{57}Fe probes. Measurements were performed in the temperature range of $10\text{ K} < T < 670\text{ K}$, wherein $\text{BiMn}_{6.96}^{57}\text{Fe}_{0.04}\text{O}_{12}$ undergoes a cascade of structural ($T_1 \approx 590\text{ K}$, $T_2 \approx 442\text{ K}$, and $T_3 \approx 240\text{ K}$) and magnetic ($T_{N1} \approx 57\text{ K}$, $T_{N2} \approx 50\text{ K}$, and $T_{N3} \approx 24\text{ K}$) phase transitions. The analysis of the electric field gradient (EFG) parameters, including the dipole contribution from Bi^{3+} ions, confirmed the presence of the local dipole moments p_{Bi} , which are randomly oriented in the paraelectric cubic phase ($T > T_1$). The unusual behavior of the parameters of hyperfine interactions between T_1 and T_2 was attributed to the dynamic Jahn–Teller effect that leads to the softening of the orbital mode of Mn^{3+} ions. The parameters of the hyperfine interactions of ^{57}Fe in the phases with non-zero spontaneous electrical polarization (P_s), including the $P1 \leftrightarrow Im$ transition at T_3 , were analyzed. On the basis of the structural data and the quadrupole splitting $\Delta(T)$ derived from the ^{57}Fe Mössbauer spectra, the algorithm, based on the Born effective charge model, is proposed to describe $P_s(T)$ dependence. The $P_s(T)$ dependence around the $Im \leftrightarrow I2/m$ phase transition at T_2 is analyzed using the effective field approach. Possible reasons for the complex relaxation behavior of the spectra in the magnetically ordered states ($T < T_{N1}$) are also discussed.

Keywords: manganites; Mössbauer spectroscopy; multiferroics; Jahn–Teller effect



Citation: Soboleva, I.S.; Nitsenko, V.I.; Sobolev, A.V.; Smirnova, M.N.; Belik, A.A.; Presniakov, I.A. Understanding Complex Interplay among Different Instabilities in Multiferroic $\text{BiMn}_7\text{O}_{12}$ Using ^{57}Fe Probe Mössbauer Spectroscopy. *Int. J. Mol. Sci.* **2024**, *25*, 1437. <https://doi.org/10.3390/ijms25031437>

Academic Editor: Takashiro Akitsu

Received: 4 January 2024

Revised: 20 January 2024

Accepted: 21 January 2024

Published: 24 January 2024



Copyright: © 2024 by the authors. Licensee MDPI, Basel, Switzerland. This article is an open access article distributed under the terms and conditions of the Creative Commons Attribution (CC BY) license (<https://creativecommons.org/licenses/by/4.0/>).

1. Introduction

The variety of structural and magnetic phase transitions in the so-called quadruple perovskite $\text{BiMn}_7\text{O}_{12}$ [1–4] and its solid solutions, such as $\text{BiMn}_{7-x}\text{Cu}_x\text{O}_{12}$ ($0 < x \leq 1.1$) [5,6], has attracted strong interest from researchers. Numerous transitions of different origins are associated with the presence of Mn^{3+} and Bi^{3+} cations in the crystal lattice of these oxides, which promotes structural instability [7–10]. High-spin Jahn–Teller (JT) cations $\text{Mn}^{3+}(d^4)$ in the non-distorted octahedral oxygen surrounding possess an energetically degenerate configuration, e_g^1 , which provokes, along with a local distortion of polyhedra (MnO_6), a cooperative interaction in which the JT centers Mn^{3+} proper, often called orbital ordering [7,8,11,12]. The distortion driven by easily polarized Bi^{3+} cations, containing the $6s^2$ lone electron pair, results in off-centric cation displacements and the formation of local electric dipoles, which are responsible for the ferroelectric properties of many Bi-containing perovskites [7,10].

Non-zero magnetization (M) co-existing with electrical polarization (P_s) is characteristic of multiferroics, which can be grouped into two types [13]. In the first group (type-I multiferroics), M and P_s are independent of each other, i.e., magnetism and ferroelectricity have different origins. In the second group (type-II multiferroics), M and P_s demonstrate a strong mutual influence, i.e., magnetism induces ferroelectricity [13]. Such a magneto-electric coupling strongly correlates with local distortions, and, thus, the roles of local polar and magnetic clusters must be studied. Therefore, these compounds are increasingly studied not only by using diffraction and magnetic methods but also using local nuclear resonance techniques, such as NMR [14–21], NQR [22,23], muon spectroscopy [24–26], the spectroscopy of perturbed angular γ – γ correlations [27,28], and Mössbauer spectroscopy [9,29,30]. The temperature dependences of hyperfine magnetic fields (B_{hf}) and principal components $\{V_{\text{ii}}\}_{X,Y,Z}$ of the tensor of the electrical field gradient (EFG) gained using these methods reproduce the corresponding dependences $M(T)$ and $P_s(T)$. Meanwhile, the relationship $B_{\text{hf}} = \alpha M$ is usually linear for ^{57}Fe , ^{55}Mn , and ^{53}Cr nuclei, and the dependencies of the EFG tensor parameters $V_{\text{ii}} = f(P_s)$ and $\eta = f'(P_s)$ (where $\eta = (V_{\text{XX}} - V_{\text{YY}})/V_{\text{ZZ}}$ is the asymmetry parameter) demonstrate nontrivial behavior. In some works, quadratic dependences $V_{\text{ii}} = a + bP_s^2$ and $\eta \propto P_s^2$ are used for approximation [31–33]. However, such an approach is rather formal and does not allow for associating the hyperfine parameters of different resonant nuclei with the structural data and physical characteristics of the compounds under study.

In the present work, we present Mössbauer-based research on the hyperfine interactions of ^{57}Fe probes in perovskite $\text{BiMn}_7\text{O}_{12}$. This manganite demonstrates spontaneous electrical polarization in the temperature range of $T < T_C \approx 440$ K, whereas, at lower temperatures ($T < T_{\text{N1}} \approx 59$ K), it acquires a magnetically ordered state and multiferroic properties [2]. In contrast to perovskites ABO_3 , in their “quadruple” analogs $(A'A''_3)\text{B}_4\text{O}_{12}$, the sublattice A is divided into two sublattices formed by cations A' with a high coordination number ($\text{CN} = 8$ – 12) and by using JT cations $A'' = \text{Cu}^{2+}$ and Mn^{3+} , which are located in the square planar oxygen coordination [34]. In the case of $(\text{Bi}^{3+}\text{Mn}^{3+}_3)[\text{Mn}^{3+}_4]\text{O}_{12}$, these sublattices consist of the cations $A' = \text{Bi}^{3+}$ and $A'' = \text{Mn}^{3+}$, whereas the sublattice with a distorted octahedral oxygen coordination (B) consists of the JT cations Mn^{3+} that directly initiate orbital ordering (cooperative JT effect) [8]. A combined effect of two cations (Mn^{3+}_B and $(\text{Bi}^{3+})_{A'}$), of which the latter contains the stereochemically active lone-pair electrons [7,9,10], results in a whole cascade of structural and magnetic phase transitions in $\text{BiMn}_7\text{O}_{12}$ (Figure 1) [3]. However, the mechanisms and driving forces of these phase transitions are still widely discussed despite abundant experimental data and theoretical studies [35].

According to the results of the earlier Mössbauer studies of perovskites $\text{AMn}_{6.96}\text{Fe}_{0.04}\text{O}_{12}$ ($A = \text{Ca}, \text{Sr}, \text{Cd}, \text{Pb}$) [35–37], the ^{57}Fe probes are localized in the structure solely in the formal oxidation state “3+”, substituting manganese cations only in octahedral sublattice. Moreover, experimental and theoretical studies show that the hyperfine parameters of the ^{57}Fe spectra reflect the features of the local crystal structure of this class of manganites. It is essential to highlight that the studies involving macroscopic diagnostic methods found the influence of the ^{57}Fe probes on physical parameters to be insignificant, as well as the patterns of the structural and magnetic transitions in these oxides. Thus, utilizing Mössbauer spectroscopy to probe a more complicated $\text{BiMn}_7\text{O}_{12}$ system is justified by the current experimental data, and the successful application of this technique is used to study other isostructural compounds of the $\text{AMn}_7\text{O}_{12}$ family.

Our work aims to qualitatively obtain new information about the local structure of $\text{BiMn}_7\text{O}_{12}$ and outline the features of the structural, electrical, and magnetic phase transitions. We describe a close interplay between the orbital and spin degrees of freedom, which is characteristic of systems with a strong electron correlation.

The Results and Discussion section of the manuscript is divided into several parts. The first part is devoted to analyzing the effect of ^{57}Fe probes on structural (T_1 , T_2 , and T_3) and magnetic (T_{N1} and T_{N2}) transitions in $\text{BiMn}_7\text{O}_{12}$ (Figure 1). Based on theoretic-

cal calculations of the EFG parameters in the paraelectric range $T > T_1$, the second part discusses the crystal chemistry of Bi^{3+} cations and their influence on the transition of the bismuth sublattice into the ordered ferroelectric state. In the third part, we consider the dynamic Jahn–Teller effect of Mn^{3+} cations in octahedral coordination at intermediate temperatures $T_2 < T < T_1$. The fourth part presents an analysis of the temperature dependence of the spontaneous polarization in $\text{BiMn}_{6.94}\text{Fe}_{0.04}\text{O}_{12}$ at temperatures $T_{N1} < T < T_3$ and $T_3 < T < T_2$. The final part describes the hyperfine magnetic interactions of ^{57}Fe probes in the magnetically ordered temperature range $T < T_{N1}$.

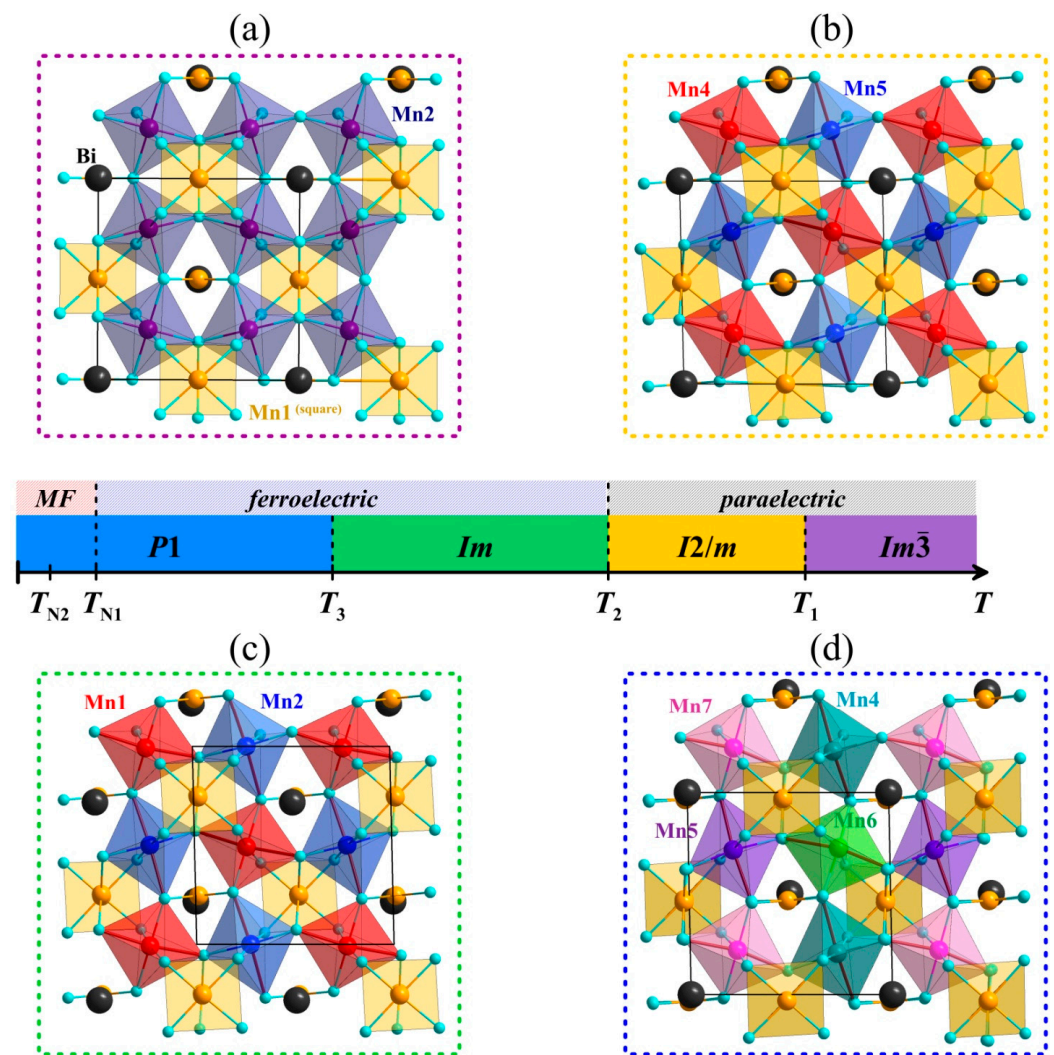


Figure 1. Crystal structures of $\text{BiMn}_7\text{O}_{12}$: (a) At $T > T_1$ in the cubic $Im\bar{3}$ structure (without Bi splitting); (b) At $T_2 < T < T_1$ in the monoclinic $I2/m$ structure; (c) At $T_3 < T < T_2$ in the monoclinic Im structure; (d) At $T < T_3$ in the triclinic $P1$ structure (all viewed along the monoclinic b axis; Elongated Mn–O bonds due to the Jahn–Teller distortions in MnO_6 octahedra are marked by red lines; The crystal cells are marked with black lined rectangles. The inset in the center depicts the accordance of the crystal structures and physical properties.

2. Results and Discussion

2.1. Crystallographic, Magnetic, and Thermodynamic Data

X-ray diffraction patterns show no additional reflections corresponding to impurity phases (Figure S1). Having been measured at different temperatures, they suggest that the studied sample retains all the crystal modifications characteristic of an undoped (without Fe) quadruple manganite $\text{BiMn}_7\text{O}_{12}$ [3]. The observed reflections at 615 K are associated with the cubic ($Im\bar{3}$) $\text{BiMn}_7\text{O}_{12}$ phase that is stable at $T > T_1$ (Figure 1a). A part of the

reflections split upon transition below T_1 , which corresponds to the monoclinic symmetry $I2/m$ (Figure 1b). The monoclinic phase reflection (242) splits upon the further cooling of the sample (Figure 1c). As noted in [3], the temperature T_3 of the phase transition monoclinic (Im) \leftrightarrow triclinic ($P1$) (Figure 1d) was not detected in the thermodynamic measurements; however, it can be evaluated from the deviation of the α and γ monoclinic unit cell angles from 90° (Figure S2). The estimated point $T_3 \approx 240$ K for $\text{BiMn}_{6.96}\text{Fe}_{0.04}\text{O}_{12}$ is noticeably lower than ~ 290 K for the undoped $\text{BiMn}_7\text{O}_{12}$ sample [3].

The $\text{BiMn}_{6.96}\text{Fe}_{0.04}\text{O}_{12}$ powder is characterized by a high degree of crystallinity according to the SEM data (Figure S3). It is inferred from particle agglomeration and the wide distribution of particle sizes ranging from 0.5 to 20 μm . Almost all crystallites have an irregular shape.

The peaks observed in the differential scanning calorimetry (DSC) curves of $\text{BiMn}_{6.96}\text{Fe}_{0.04}\text{O}_{12}$ (Figure 2a) correspond to the phase transitions at the temperatures $T_1 \approx 580\text{--}590$ K and $T_2 \approx 420\text{--}440$ K, i.e., structural transitions $I2/m \leftrightarrow Im\bar{3}$ and $Im \leftrightarrow I2/m$, respectively, according to the literature data [3]. It is worth noting that the undoped sample $\text{BiMn}_7\text{O}_{12}$ demonstrated the same transitions at ~ 608 K and ~ 460 K, respectively, as was reported in the earlier experiments [3]. Further lowering the lattice symmetry to $P1$ does not affect DSC curves. Measurements upon cooling and heating reveal a difference in the transition points $\Delta T_1 \sim 7$ K and $\Delta T_2 \sim 20$ K, both of which slightly exceed the corresponding values for the $\text{BiMn}_7\text{O}_{12}$ sample [3].

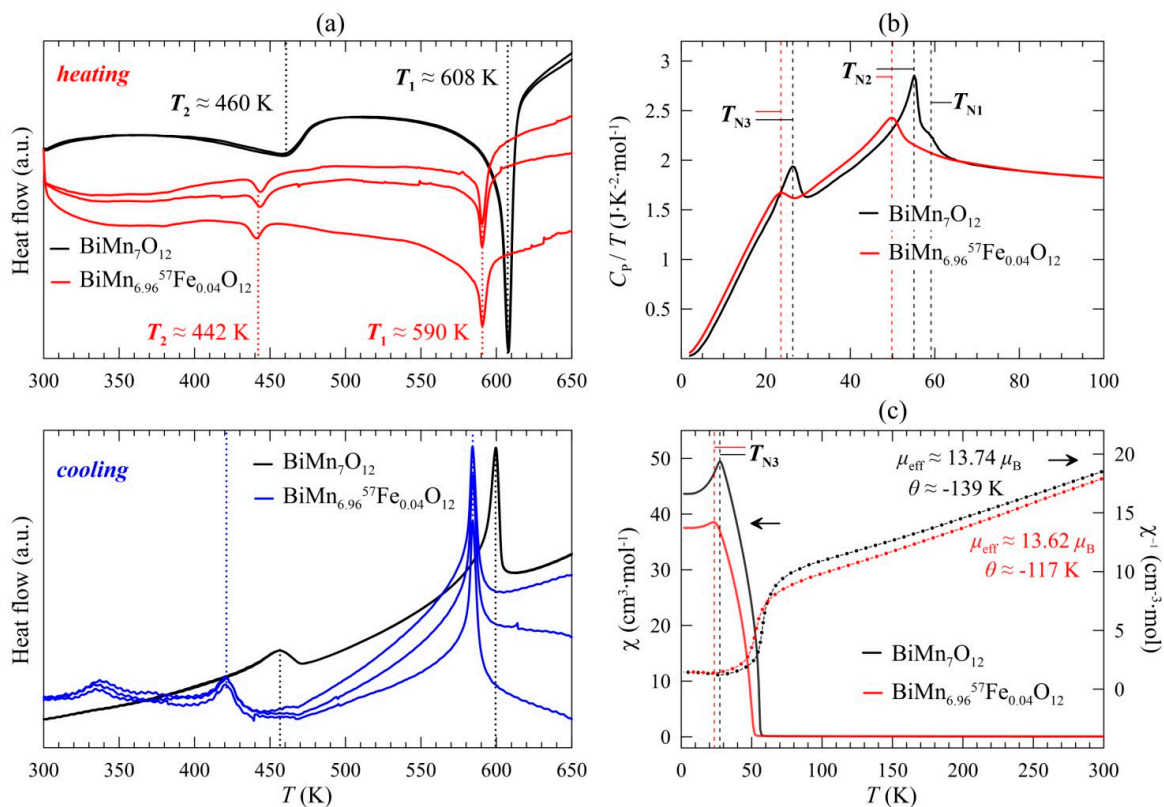


Figure 2. (a) Differential scanning calorimetry (DSC) curves of $\text{BiMn}_{6.96}\text{Fe}_{0.04}\text{O}_{12}$ upon heating and cooling (three runs were performed to check the reproducibility; since there were no peaks observed, data in the 125–300 K range are not shown); (b) Specific heat, plotted as C_p/T versus T , of $\text{BiMn}_7\text{O}_{12}$ and $\text{BiMn}_{6.96}\text{Fe}_{0.04}\text{O}_{12}$ at $H = 0$ (measurements were performed on cooling); (c) ZFC dc (left scale) and reversed (right scale) magnetic susceptibility curves of $\text{BiMn}_7\text{O}_{12}$ and $\text{BiMn}_{6.96}\text{Fe}_{0.04}\text{O}_{12}$ (dashed vertical lines emphasize magnetic anomalies).

By measuring the heat capacity $C_p/T(T)$ in $\text{BiMn}_{6.96}\text{Fe}_{0.04}\text{O}_{12}$ (Figure 2b), we obtained the values of the temperatures of transition to the magnetically ordered states T_{N2} and T_{N3} . T_{N2} reached ~ 50 K, and the temperature of the third magnetic transition $T_{N3} \approx 24$ K was

3–5 K lower than that of the undoped manganite [4]. The third phase transition at T_{N3} is also clearly seen in the temperature profile of the magnetic susceptibility $\chi(T)$ and is typical of antiferromagnets (Figure 2c). The parameters of the Curie–Weiss fit (Figure 2c) are in good agreement with the data obtained for the undoped manganite $\text{BiMn}_7\text{O}_{12}$ [3]. The temperature shift of structural and magnetic transitions upon iron-doping can be caused by the stabilization of a small quantity of iron in the manganite structure, rather than the precipitation of an impurity iron phase or its localization on the crystallite surface.

2.2. Mössbauer Data for $T > T_1$

Figure 3a represents the typical Mössbauer spectra of ^{57}Fe in $\text{BiMn}_{6.96}\text{Fe}_{0.04}\text{O}_{12}$ measured at high temperatures $T > T_1$. At these temperatures, the spectra consist of a quadrupole doublet with small and virtually temperature-independent splitting $\Delta \approx 0.26$ mm/s (Figure 4). The value of the isomer shift $\delta_{633\text{K}} \approx 0.16$ mm/s corresponds to Fe^{3+} cations [38], isovalently substituting Mn^{3+} in the octahedral positions of Mn2 (Figure 1a). Despite $\text{BiMn}_{6.96}\text{Fe}_{0.04}\text{O}_{12}$ having a cubic structure ($Im\bar{3}$) at $T > T_1$ and the local octahedral anion environment of the Mn2 sites being formally considered to be undistorted, the local symmetry of the oxygen sites explains the non-zero quadrupole splitting of the spectrum (Table 1). Although all the Mn2 sites substituted by Fe^{3+} probes are equivalent, the experimental spectra cannot be satisfactorily fitted using one doublet with unbroadened resonant lines. This suggests the presence of a distribution $p(\Delta)$ of Δ values (Figure 3a), i.e., that the crystalline environment of the ^{57}Fe probes is not homogenous.

Table 1. ^{57}Fe hyperfine parameters at $T > T_1$ of $\text{BiMn}_{6.96}\text{Fe}_{0.04}\text{O}_{12}$.

T, K	$\langle\delta\rangle, \text{mm/s}$	$\langle\Delta\rangle, \text{mm/s}$	$D_p^{\text{exp}}, \text{mm}^2/\text{s}^2$	$\Gamma, \text{mm/s}$
602	0.18(1)	0.28(1)	0.016(1)	0.24 *
622	0.17(1)	0.26(1)	0.016(1)	0.24 *
633	0.16(1)	0.26(1)	0.017(1)	0.24 *
653	0.15(1)	0.25(1)	0.016(1)	0.24 *

* When processing the spectra, the linewidth Γ was fixed in accordance with the “thin” absorber and properties of the source. $\langle\delta\rangle$ is the mean isomer shift, $\langle\Delta\rangle$ is the mean quadrupole splitting, D_p^{exp} is the dispersion of the quadrupole splitting taken from the distribution reconstruction procedure.

The EFG parameters were calculated within the “ionic model” to support this assumption. It takes into account monopole (V_{ZZ}^{mon}) and dipole (V_{ZZ}^{dip}) contributions from ions that are located in the non-centrosymmetric sites in $\text{BiMn}_7\text{O}_{12}$. Having stereochemically active $6s^2$ lone-pair electrons, Bi^{3+} cations are considered to mainly contribute to V_{ZZ}^{dip} . The lone pair induces the displacement of Bi^{3+} cations from their centrosymmetric positions, which is equivalent to inducing the electric dipole moment p_{Bi} . Therefore, only dipole contributions ($V_{ZZ,\text{Bi}}^{\text{dip}}$) from Bi^{3+} were taken into account when calculating V_{ZZ}^{dip} using variable p_{Bi} values in further calculations. Additionally, the dipole moments p_{Bi} were considered to be randomly oriented in a crystal lattice since $\text{BiMn}_7\text{O}_{12}$ is paraelectric at $T > T_1$ [3]. See Appendix A for details.

The inclusion of the dipole contribution from Bi^{3+} allows us to achieve a good agreement between the theoretical and experimental values of the quadrupole splitting. The calculated dipole moment $p_{\text{Bi}} \approx 1.2 \times 10^{-29}$ C·m lays within the range of the corresponding values p_{Bi} for other Bi^{3+} oxide compounds [10]. Most importantly, even with a random orientation of the p_{Bi} moments, the Mn2 sites become non-equivalent in terms of the induced lattice contribution $V_{ZZ,\text{Bi}}^{\text{dip}}$. This is, in essence, the main cause of the observed broadening of the spectra, i.e., the appearance of the $p(\Delta)$ distribution (Figure 3a). Using the calculated values of Δ^{theor} for each Mn2 site within the P1 pseudocell (see Appendices A–C), which is characterized by the peculiar relative orientation of the surrounding dipole moments p_{Bi} , we calculated the mean value of the quadrupole splitting as well as the dispersion $D_p^{\text{theor}} = 0.020$ mm²/s², which was found to be close to $D_p^{\text{exp}} \approx 0.017$ mm²/s² of the experimental (Table 1) distribution $p(\Delta)$.

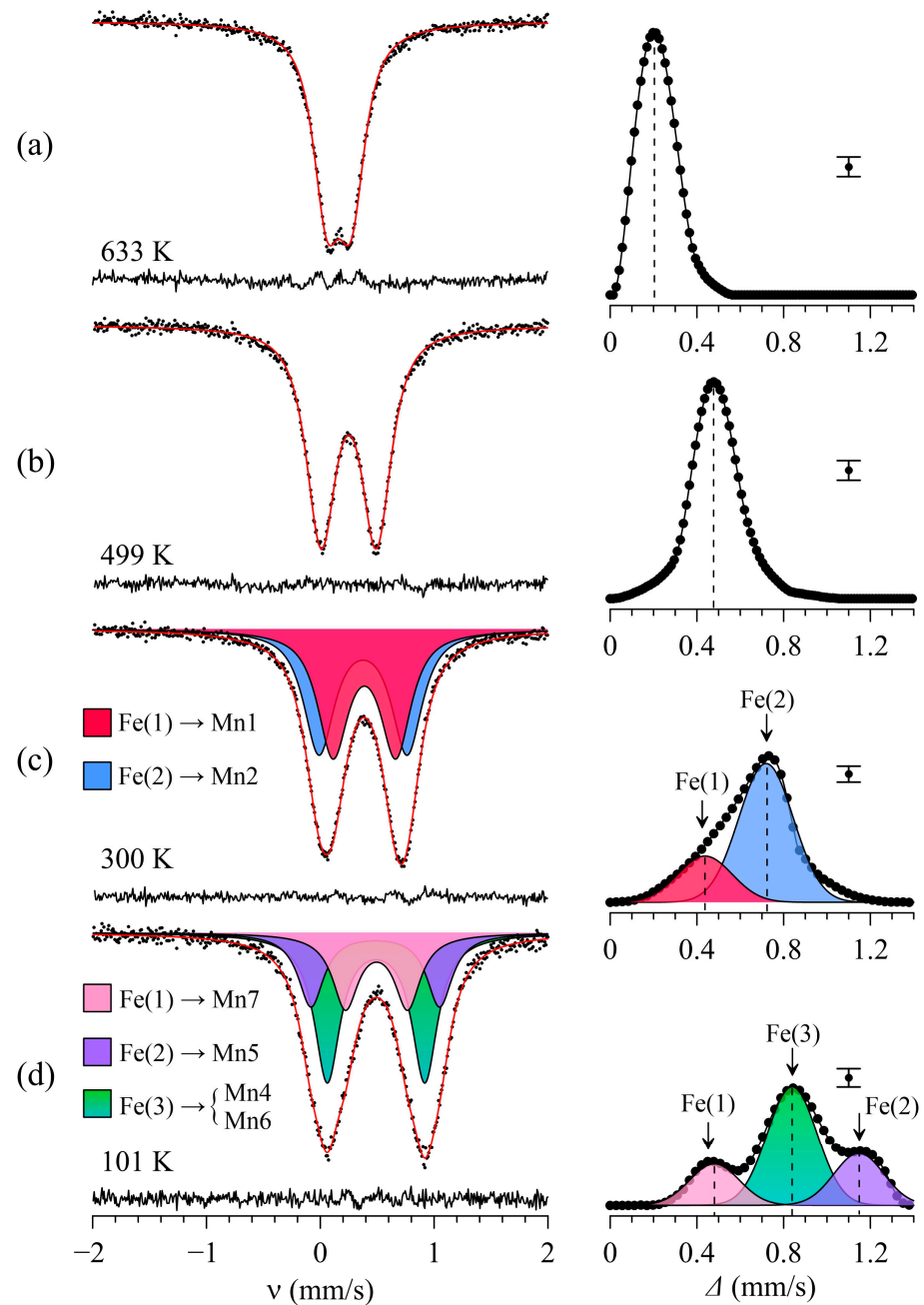


Figure 3. Left panel: typical Mössbauer spectra of the ^{57}Fe nuclei in $\text{BiMn}_{6.96}\text{Fe}_{0.04}\text{O}_{12}$ manganite measured at different temperatures (each at a specific range according to different crystal structures). Right panel: the $p(\Delta)$ distributions and their representation as the superposition of normal distributions corresponding to the crystal sites of ^{57}Fe probe nuclei within a manganite structure. (a–d) Correspond to particular temperature range (see text).

Thus, the Mössbauer data indicate that, in the paraelectric cubic phase of $\text{BiMn}_{6.96}\text{Fe}_{0.04}\text{O}_{12}$ at $T > T_1$, Bi^{3+} cations exist in a locally distorted environment and retain their electric dipole moments p_{Bi} that are randomly oriented in the cubic lattice. In this case, transitions to the anti- or ferroelectric states at lower temperatures $T < T_2$ should be accompanied by the ordering of the p_{Bi} dipoles, i.e., they should represent the “order-disorder” phase transitions [39], as an alternative to the “displacive” phase transitions [40]. Previously, in refs. [41,42], static dipole moments p_{Bi} are assigned to the lone sp^x -hybrid electron pairs of Bi^{3+} cations, which are oriented parallel to the direction of the displacement of a bismuth cation from its conventional centrosymmetric site (Figure 5a). Such an

approach can qualitatively explain the unusually large thermal ellipsoids of Bi^{3+} cations reported in [1,3] for $\text{BiMn}_7\text{O}_{12}$ at $T > T_1$. These ellipsoids may form as a result of the superposition of multidirectional sp^x -hybrid pairs, whose randomly oriented lobes create a sphere that manifests itself in the diffraction patterns as unusually large bismuth thermal ellipsoids (Figure 5b). However, it should be noted that this approach is a simplified, albeit illustrative, model that has not been experimentally confirmed for the majority of known Bi(III) phases [43–45].

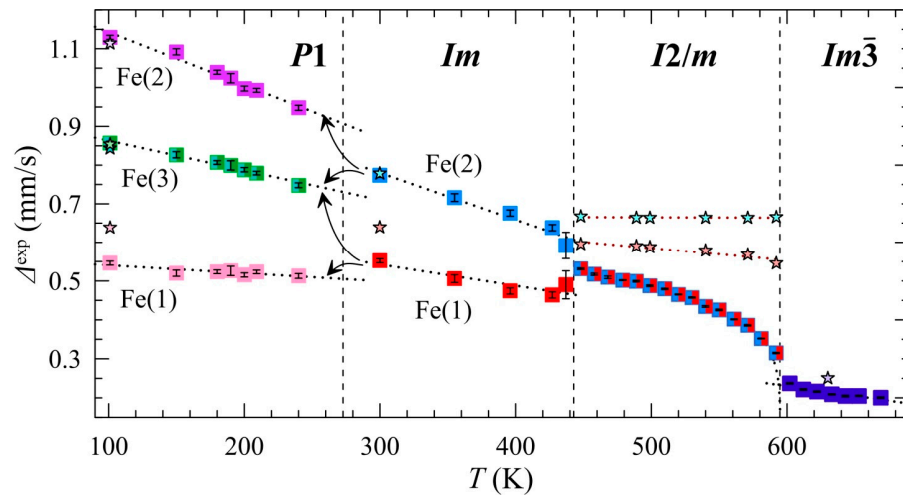


Figure 4. The temperature dependencies of the experimental values of the quadrupole splittings $\Delta_i^{\text{exp}}(T)$ of the partial Fe(i) spectra at specific ranges according to different crystal structures of the $\text{BiMn}_{6.96}\text{Fe}_{0.04}\text{O}_{12}$ manganite (asterisks show the theoretical values).

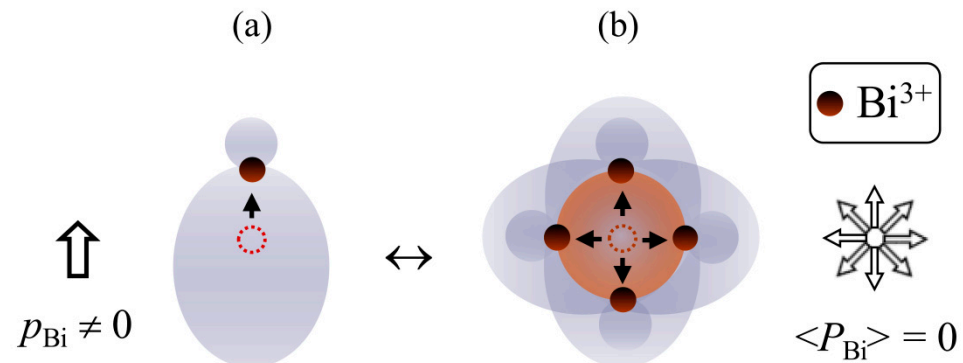


Figure 5. Schematic representations: (a) the formation of the p_{Bi} dipole moment as a result of the displacement of Bi^{3+} cations (brown balls) from their centrosymmetric positions (balls with a dotted line). The Bi^{3+} center is shifted toward the lone pair; (b) the random orientation of the lone electron pairs or displacements of Bi^{3+} cations leads to the zero value of the total crystal polarization ($\langle P_{\text{Bi}} \rangle$) averaged over all directions (the large brown ball represents the ellipse of the thermal vibrations of bismuth).

2.3. Mössbauer Data for $T_2 < T < T_1$

$\text{BiMn}_{6.96}\text{Fe}_{0.04}\text{O}_{12}$ undergoes the structural transition at $T_1 \approx 590$ K, transforming from cubic ($Im\bar{3}$) to monoclinic ($I2/m$) lattice symmetry (Figure 1b) with decreasing temperature. Figure 3b illustrates a typical Mössbauer spectrum of ^{57}Fe probes in the monoclinic $\text{BiMn}_7\text{O}_{12}$, which has the shape of a symmetrically broadened quadrupole doublet. Despite the lowering of the manganite lattice symmetry, the obtained distributions $p(\Delta)$ show a single maximum that corresponds to the average $\langle \Delta \rangle$ value which increases drastically upon decreasing temperature (Figures 3 and 4). Considering the fact that the main contribution to the EFG imposed on the spherical Fe^{3+} cations is accounted for by the distortion of their

crystalline surrounding (lattice contribution), it is difficult to explain the observed sharp change in the quadrupole splitting with temperature.

The results of the calculation of the EFG parameters for the different sites of Mn^{3+} with the monopole contributions from all ions (Bi^{3+} , Mn^{3+} , and O^{2-}), as well as additional dipole contributions from Bi^{3+} and O^{2-} , show that the values $V_{ZZ,\text{Mn}4} = 3.76 \times 10^{20} \text{ V/m}^2$ and $V_{ZZ,\text{Mn}5} = 4.21 \times 10^{20} \text{ V/m}^2$ are close to each other, which is probably responsible for the presence of only one maximum in $p(\Delta)$ (Figure 3b). As expected, the EFG parameters for both Mn sites are almost independent of temperature. Moreover, it was established that the calculated values $\Delta_{\text{Mni}}^{\text{theor}} \approx eQV_{ZZ,\text{Mni}}^{\text{teop}}$ for sites Mn4 and Mn5 (where Q is the quadrupole moment of ^{57}Fe nuclei) remarkably exceed the corresponding experimental values Δ^{exp} (Figure 4; Tables S2–S5).

We suppose that the abovementioned discrepancy between the calculated and experimental values of the quadrupole splitting ($\Delta^{\text{theor}} > \Delta^{\text{exp}}$) and their unusually strong temperature dependences can be attributed to the dynamic JT effect of Mn^{3+} cations occurring in this temperature range [46]. The JT interactions of the Mn^{3+} cations in $\text{BiMn}_7\text{O}_{12}$ can result in the so-called orbital ordering, or cooperative JT effect, which is also observed in other perovskite-like Mn(III) oxide systems, namely, RMnO_3 [47,48], $\text{R}_{1-x}\text{A}_x\text{MnO}_3$ [11], and $\text{AMn}_7\text{O}_{12}$ [37,49] ($R = \text{REE}$, $A = \text{Ca, Sr, Pb}$). All these systems can exhibit a structural transition to a crystal lattice with enhanced symmetry in the temperature range $T > T_{\text{JT}}$, which is ascribed to the dynamic JT effect, or the “melting” of the cooperative JT distortion [46]. Similar phase transitions can occur through two mechanisms: one involves increasing the symmetry of distorted (Mn^{3+}O_6) polyhedra until the uniform population of Mn^{3+} e_g -orbitals is achieved, and the other entails the orientational disordering of distorted (Mn^{3+}O_6) polyhedra while preserving the polarization of e_g -orbitals even at high temperatures ($T \gg T_{\text{JT}}$) [50]. As was noted in several refs. [51–53], the local disordering of (Mn^{3+}O_6) polyhedra can start at a temperature (T^*) that is significantly lower than the temperature of the structural phase transition T_{JT} ($\gg T^*$). However, there is still no reliable experimental data on the changes in the structure and electronic state of manganite, which take place in this “intermediate” temperature range.

Local minima are known to appear on the adiabatic potential surface of possible nuclear configurations of O^{2-} anions in the (MnO_6) polyhedra if the anharmonicity of vibronic interactions is taken into account. These minima reflect the specific orthorhombic distortions of the corresponding polyhedra. With increasing temperature, the crystalline environment of the JT Mn^{3+} cations stochastically relaxes between these minima due to thermally activated excitations or the tunnel effect [54]. Although the Fe^{3+} cations per se do not participate in the vibronic interactions, their local crystal environment also fluctuates dynamically due to the cooperative JT effect. Therefore, we suggest that the observed significant reduction in the Δ^{exp} values compared to the theoretical calculations can be associated with the relaxation behavior of the Mössbauer spectra in the temperature range $T_2 < T < T_1$. In [54,55], it was shown that such spectra can be described with the “two-level model” in the limit of “fast relaxation”, i.e., when $\Omega_R \gg \Omega_0$, where Ω_R and Ω_0 are the frequencies of the relaxation of the oxygen environment and the precession of the ^{57}Fe quadrupole moment around the V_{ZZ} direction, respectively. The model adopts the frequencies of forward (Ω_{12}) and reverse (Ω_{21}) transitions between states “1” and “2” as variables connected by the detailed equilibrium principle $n_1\Omega_{12} = n_2\Omega_{21}$, where n_1 and n_2 are the populations of states (Figure 6a) [55].

In the monoclinic structure ($I2/m$) of $\text{BiMn}_7\text{O}_{12}$, the distortion of (MnO_6) polyhedra corresponding to the energy minimum E_1 of the adiabatic potential, is described as a “bonding” $Q^{(-)}$ —the linear combination of the orthorhombic (Q_2) and tetragonal (Q_3) vibrational modes [7,56]. In this case, the distortion with a higher energy E_2 is attributed to the “antibonding” vibration mode $Q^{(+)}$. In a local approximation, when only the closest anion environment is considered, the two vibrational modes— $Q^{(-)}$ and $Q^{(+)}$ —correspond to the distortions that exhibit equal magnitudes but opposite signs in their EFG components (V_{ZZ}) imposed on the ^{57}Fe nuclei occupying the Mn4 and Mn5 sites [54]. Consequently, when the

population of the E_1 and E_2 levels equalizes with increasing temperature, quadrupole splitting sharply decreases, i.e., $\Delta(T) \propto \langle V_{ZZ} \rangle$, where $\langle V_{ZZ} \rangle$ is averaged over the energy states E_1 and E_2 [54]. On the other hand, the monotonous decrease in $\Delta(T)$ up to T_1 can suggest a gradual enhancement of the (FeO_6) symmetry upon approaching the temperature of the structural phase transition $I2/m \rightarrow Im\bar{3}$. This conclusion is consistent with the synchrotron X-ray diffraction studies of $\text{BiMn}_7\text{O}_{12}$, which also demonstrate the gradual decrease in the distortion parameter Δ_d of (MnO_6) polyhedra when $T \rightarrow T_1$ [3]. Thus, these parameters behave similarly when assessed by inherently different characterization techniques. These data suggest the second-order JT phase transition that can be referred to as the displacive structural transition, in contrast to the “order-disorder” transition mechanism.

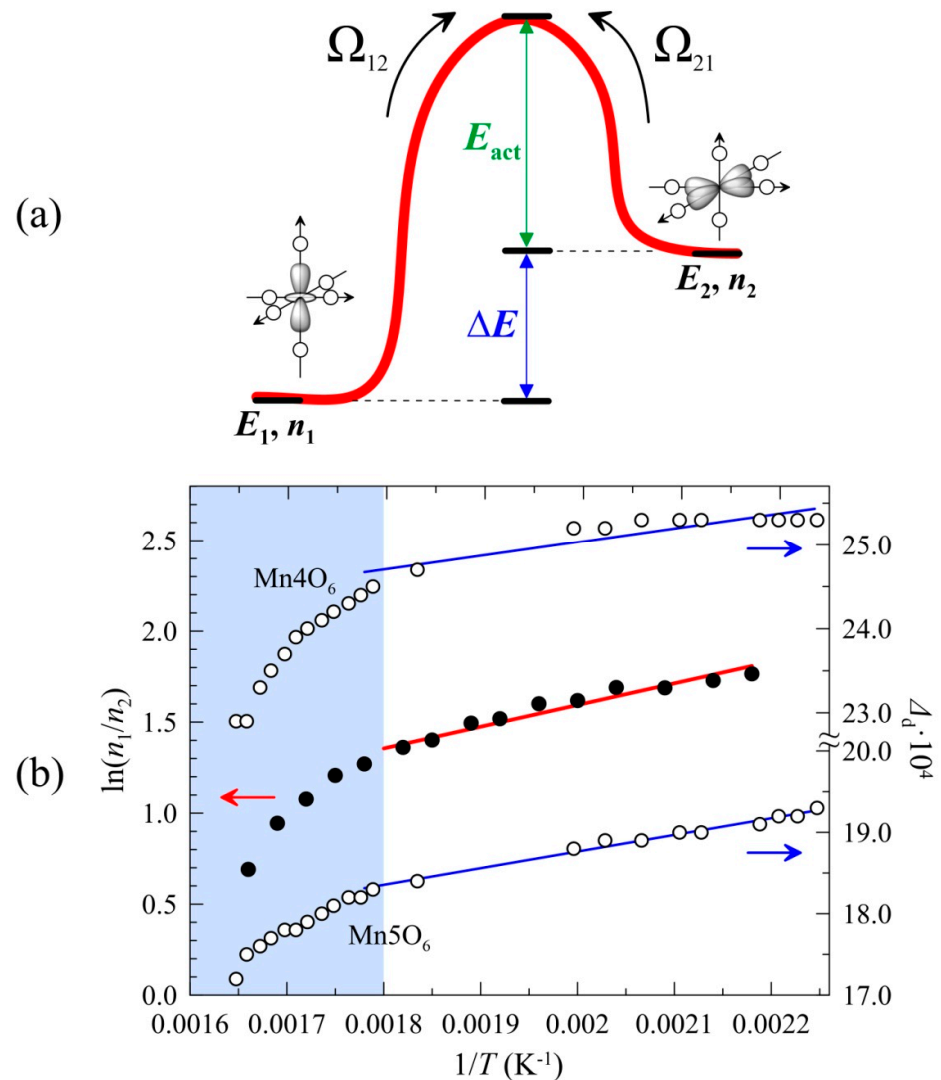


Figure 6. (a) The explicative scheme of the two-level relaxation model: E_i —the energies of states “1” and “2”, n_i —the probabilities of states, Ω_{ij} —the frequencies of transitions between states. (b) The reciprocal temperature dependencies of the logarithm $\ln(n_1/n_2)$ of probabilities n_1 and n_2 ratio, and the distortion parameters Δ_d for Mn_4O_6 and Mn_5O_6 octahedra, calculated from structural data [3]. Blue lines represent the linear approximation in the selected temperature range and are shown for visual convenience. The shaded part corresponds to the temperature range ($T > 500$ K) for which a change in the degree of the distortion (Δ_d) of the MnO_6 polyhedra is expected and, as a consequence, so too is a change in the relative position of the energy levels E_1 and E_2 (see text) The black dots correspond to the left scale, and the circles correspond to the right scale.

The fitting of the whole series of spectra within the framework of a two-level model allowed us to estimate the average relaxation frequency $\Omega_R = \Omega_{12}\Omega_{21}/(\Omega_{12} + \Omega_{21}) \approx (2-7) \times 10^7$ Hz, which significantly exceeds the frequency of the quadrupole precession $\Omega_0 \approx 8.5 \times 10^6$ Hz. Increasing temperature leads to a gradual equalization of the populations n_1 and n_2 . This should result in a sharp decrease in the quadrupole splitting and a slight broadening of the doublet components in the limit of fast relaxation $\Omega_R \gg \Omega_0$. Indeed, this pattern describes the temperature-related changes of all the spectra at $T_2 < T < T_1$ (Figure S4). Using the linear approximation of $\ln(n_1/n_2) = f(1/T)$ (obtained from the Arrhenius equation):

$$\Omega_{12(21)}(T) = \Omega_{1(2)}^0 \exp\left(-\frac{E_{12(21)}}{k_B T}\right),$$

where $\Omega_{1(2)}^0$ are temperature-independent parameters; $E_{12(21)}$ are the activation energies of “1” and “2” states, respectively; k_B is the Boltzmann constant) we evaluated the energy difference between the relaxed states $\Delta E = 69(2)$ meV and the mean value of the activation energy $E_{act} = 220(9)$ meV (Figures 6a and S5) that closely corresponds to $\langle E_{act} \rangle$ for other perovskite-like Mn(III) manganites [57]. However, a deviation from linearity is observed at higher temperatures ($T > 550$ K) (Figure 6b). This is likely to result from the changes in the relative position of levels E_1 and E_2 between which the relaxation occurs. This explanation is indirectly supported by a similar temperature profile of the distortion parameters Δ_d of polyhedra (MnO_6) (Figure 6b), which govern the splitting of the $3d$ levels of Mn cations under the influence of the ligand field.

It is worth noting that the observed structural changes in $\text{BiMn}_7\text{O}_{12}$ in the temperature range of the JT transition are similar to those in the isostructural phase of $\text{LaMn}_7\text{O}_{12}$ [58] but differ crucially from the so-called “traditional” perovskites RMnO_3 ($R = \text{REE}$), in which the cooperative JT effect follows the “order-disorder” mechanism [39]. In these oxides, polyhedra (Mn^{3+}O_6) remain distorted even at temperatures significantly exceeding T_{JT} . However, these distortions are randomly oriented in the crystal lattice, thus making the structure “macroscopically” more symmetrical compared to the low-temperature phase with orbital ordering.

2.4. Mössbauer Data for Temperature Ranges $T_3 < T < T_2$ and $T_{N1} < T < T_3$

In the temperature range $T_3 < T < T_2$, the Mössbauer spectra of $\text{BiMn}_{6.96}\text{Fe}_{0.04}\text{O}_{12}$ consist of a broadened quadrupole doublet (Figure 3c). The observed bimodal profile of $p(\Delta)$ (Figure 3c) suggests the stabilization of ^{57}Fe nuclei at two different crystallographic sites of the manganite. This conclusion agrees with the earlier structural data for $\text{BiMn}_7\text{O}_{12}$ [3]: in the crystal lattice with the Im symmetry, the JT Mn^{3+} cations occupy two sites, Mn1 and Mn2, in the very distorted octahedral oxygen environment (Figure 1c). Thus, the high value $\langle \Delta \rangle \approx 0.62$ mm/s observed in the spectra of Fe^{3+} probe cations is conditioned by a low symmetry of the oxygen environment of the JT Mn^{3+} cations. Based on the $p(\Delta)$ distribution, we fitted the whole series of spectra measured in the range $T_3 < T < T_2$ as a superposition of two quadrupole doublets, Fe(1) and Fe(2), having close values of isomer shifts, $\delta_1 \approx \delta_2$ (Figure 3c).

The analysis above yielded anomalously sharp temperature dependences $\Delta_i(T)$ for both Fe(1) and Fe(2) doublets (Figure 4). Such behavior can stem from the induction of spontaneous $\text{BiMn}_7\text{O}_{12}$ polarization at $T < T_2$ [3]. To support this assumption quantitatively, we obtained an expression relating the lattice contributions V_{ZZ}^{lat} with the values and mutual orientation of electric moments (\mathbf{p}_k) in the lattice of $\text{BiMn}_7\text{O}_{12}$ (for details, see SI). The values \mathbf{p}_k and their projections p_{ik} were calculated using the Born model [59]: $\mathbf{p}_k = Z_k \Delta \mathbf{r}_k$ or $p_{ik} = Z_k \Delta x_{ik}$, where Z_k is the Born charge of the k th ion, which is an isotropic scalar value in our calculation; $\Delta \mathbf{r}_k$ (Δx_{ik}) is the vector of the displacement of the k th ion (and i th projection) from the centrosymmetric position. The values $\Delta \mathbf{r}_{kk}$ and Δx_{ik} were calculated using the crystallographic data for $\text{BiMn}_7\text{O}_{12}$ obtained at 300 K [3]. To estimate Born charges, we sequentially varied the charges $\{Z_{\text{Bi}}, Z_{\text{Mn}(i)}, Z_{\text{O}(i)}\}$ and their corresponding

dipole moments p_{ik} with the given displacement Δx_{ik} until the best agreement with the experimental splitting Δ_i was achieved (Table S1). The values approximated in such a manner that $Z_{Bi} = +3.30$, $Z_{Mn1} \approx Z_{Mn2} = +3.30$, and $Z_O = -2.20$, and all lie within the range of the Born charges obtained earlier for the corresponding ions in other perovskite oxides [60].

Using the above approximations, we derived an equation that describes $\Delta(T)$ as a function of the i th projections $\{P_i\}_{i=x,y,z} = \sum_k p_{ik}$ of the spontaneous polarization $P_s = (P_x^2 + P_y^2 + P_z^2)^{1/2}$:

$$\Delta(T) = (1 - \gamma_\infty) \frac{eQ}{2} \sum_k \frac{\partial^2}{\partial x_i^2} \left[\frac{q_k}{r_k} + \frac{r_{ik} P_i(T)}{r_k^3} \left(\frac{p_k(T_0)}{P_s(T_0)} \right) \right] \quad (1)$$

where $p_k(T_0)/P_s(T_0)$ is the ratio of the dipole moment of the k th ion (p_k) to the spontaneous polarization in the crystal, which is calculated based on the crystallographic data for $\text{BiMn}_7\text{O}_{12}$ (*Im*). The first and the second terms in Equation (1) are the monopole and dipole contributions to the EFG. Using Equation (1), we plotted theoretical dependencies $\Delta_1(P_s)$ and $\Delta_2(P_s)$ (Figure 7). Using the numerical solution of the equations $\Delta_1(P_s) = \Delta_1(T)$ and $\Delta_2(P_s) = \Delta_2(T)$ and accounting for statistical errors allowed us to simulate the temperature dependence $P_s(T)$ (Figure 8).

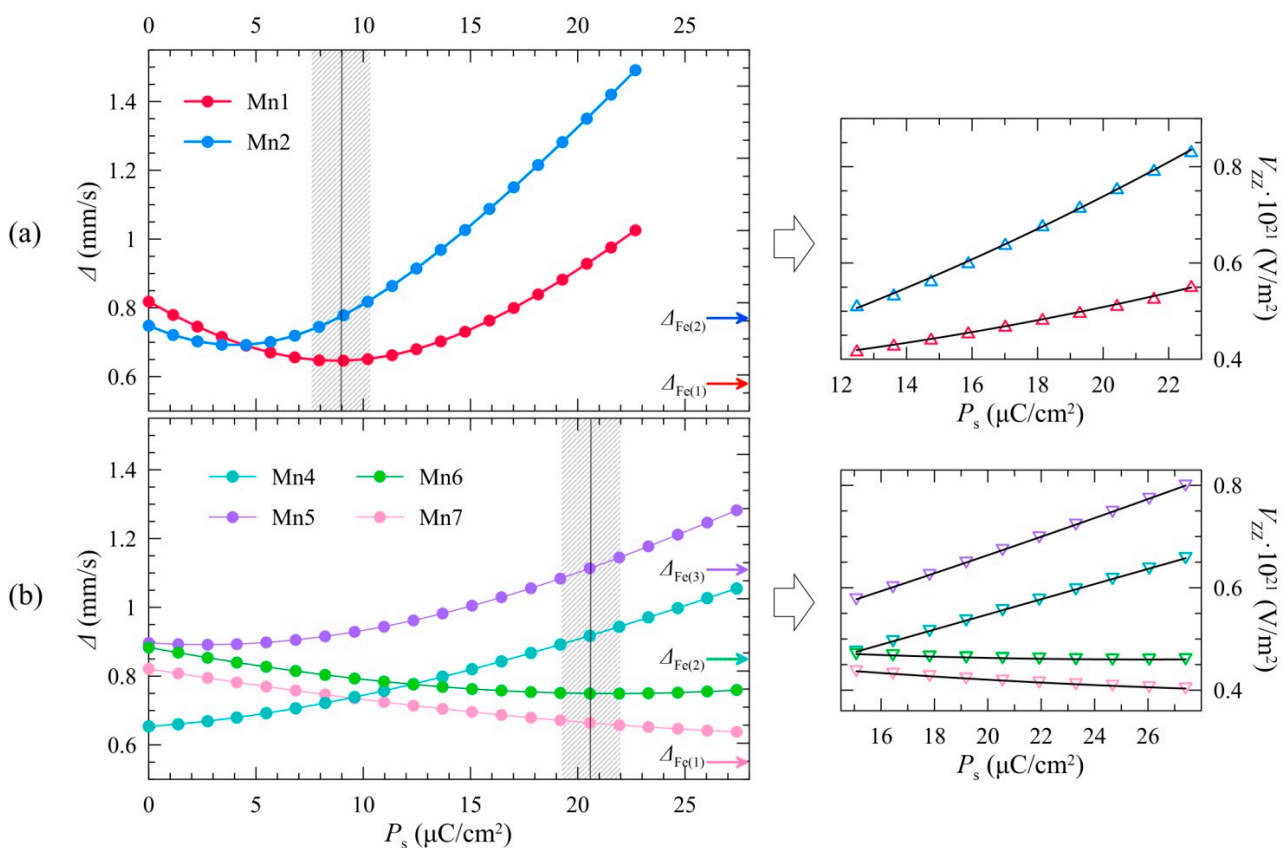


Figure 7. Left panel: The dependencies of the theoretical Δ_i values versus spontaneous crystal polarization P_s at (a) $T = 300$ K and (b) $T = 10$ K. The curves refer to the experimental values Δ_i^{exp} from the Mössbauer spectroscopy data at (a) 300 K and (b) 101 K temperatures. Shaded areas correspond to evaluated P_s values when the theoretical $\Delta_i(P_s)$ values conform to the experimental Δ_i^{exp} ones in the best way. The vertical lines in the shaded areas showed the approximate mean position for ease of perception. Right panel: the dependencies of the theoretical V_{ZZi} values versus spontaneous crystal polarization P_s at corresponding temperatures fitted with quadratic functions (see text).

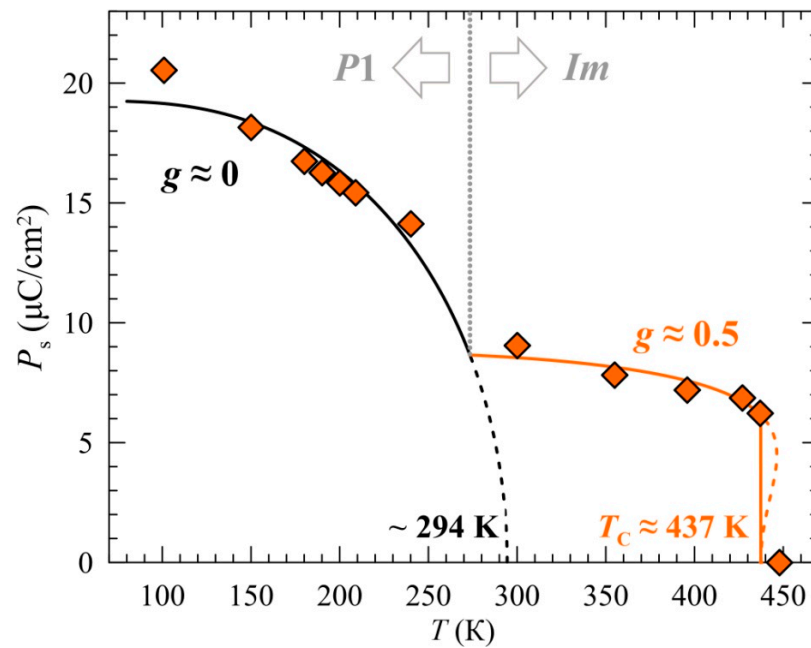


Figure 8. The temperature dependencies of the spontaneous polarization $P_s(T)$ for the two crystal structures of the $\text{BiMn}_{6.96}\text{Fe}_{0.04}\text{O}_{12}$ manganite. The solid and dashed curves represent the fitting in order with theory explained in the text. The dotted line shows the temperature of the phase transition.

The same algorithm for constructing dependencies $P_s(T)$ using experimental data $\Delta_i(T)$ was applied to the triclinic phase (P1) of $\text{BiMn}_7\text{O}_{12}$. The distribution $p(\Delta)$ has a trimodal profile for the given structure modification (Figure 3d), which indicates that Fe^{3+} cations occupy at least three nonequivalent sites. According to the structural data [4], the Mn^{3+} cations form four equally populated sites (Mn4, Mn5, Mn6, and Mn7) in an octahedral oxygen environment (Figure 1d). The calculated EFG parameters of Mn4 and Mn6 suggest that these atoms are located symmetrically near similar crystalline environments, making them indistinguishable in the ^{57}Fe Mossbauer spectra. Therefore, the spectra at $T_{N1} \leq T \leq T_3$ were fitted with three quadrupole doublets, namely, Fe(1), Fe(2), and Fe(3), with the Fe(3) component being two times more intense than Fe(1) and Fe(2) (Figure 3d). Using the structural data for the triclinic $\text{BiMn}_7\text{O}_{12}$ phase at 10 K [4] and the described algorithm combining the theoretical dependencies $\Delta_i(P_s)$ with the experimental $\Delta_i(T)$ values, we were able to model $P_s(T)$ across the temperature range under investigation (Figure 8).

The dependences $\Delta \propto V_{ZZ} = f(P_s)$ (Figure 7) agree with the results of [24–27], where, in a general case, the dependence of $V_{ZZ}(P_s)$ at low P_s values was represented using a Taylor series expansion:

$$V_{ZZ}(P_s) = V_{ZZ}^{(0)} + \sum_i \left(\frac{\partial V_{ZZ}}{\partial x_i} \right) P_s + \frac{1}{2} \sum_{i,j} \left(\frac{\partial^2 V_{ZZ}}{\partial x_i \partial x_j} \right) P_s^2 + \dots = V_{ZZ}^{(0)} + \alpha P_s + \beta P_s^2 + \gamma P_s^4 \dots \quad (2)$$

It was shown in [12] that the linear term vanishes and the quadratic term in the expansion becomes significant ($\beta \gg \gamma \neq 0$) for the centrosymmetrical crystal sites. At the same time, if the center of symmetry is absent, the linear term should be predominant ($\alpha \gg \beta \gg \gamma \neq 0$). Since for both polymorphic modifications of the $\text{BiMn}_7\text{O}_{12}$ octahedral Mn^{3+} sites are not centrosymmetric, the above dependences $V_{ZZ}(P_s)$ can be described using an expansion in a series with nonzero parameters α and β , whose values (Table 2), in order of magnitude, are consistent with similar data from other perovskite-like ferroelectrics [24–27].

Table 2. Taylor expansion parameters $V_{ZZ}^{(0)}$, α , and β of the dependences $V_{ZZ}(P_s)$ calculated for both polymorphic modifications for all octahedral Mn^{3+} sites.

T, K	Site	$V_{ZZ}^{(0)}$ ($V/m^2 \times 10^{21}$)	α ($V/C \times 10^{21}$)	β ($V \cdot m^2/C^2 \times 10^{22}$)
300	Mn1	0.38(1)	−0.6(1)	0.78(3)
	Mn2	0.27(1)	1.9(1)	0.48(2)
101	Mn4	0.385(1)	0.71(1)	0.12(3)
	Mn5	0.519(3)	0.39(2)	0.24(6)
	Mn6	0.565(1)	−0.85(1)	0.195(1)
	Mn7	0.526(1)	−0.72(1)	0.100(1)

When describing the dependences, $P_s(T)$ was obtained for two temperature ranges, and we used the model of the average effective field [61]. Within the framework of this approach, it is assumed that every ion in the ferroelectric crystal is affected by an effective electric field (E_{eff}), which can be expressed as

$$E_{\text{eff}} = E_0 + \beta P_s + \gamma P_s^3 + \delta P_s^5 + \dots \quad (3)$$

where E_0 is the external electrical field, and the following terms correspond to the dipolar, quadrupolar, and octupolar interactions, respectively. In our calculations, $E_0 = 0$. Moreover, only dipolar and quadrupolar interactions were taken into consideration, the latter (γ) serving to describe the phase transitions of both the first and second orders within the united approach. For statistical consideration, the $P_s(T)$ dependence of polarization can have a general form [61]:

$$P_s(T) = P_0 \tanh\left(\frac{E_{\text{eff}} P_0 N^{-1}}{k_B T}\right) = P_0 \tanh\left(\frac{(\beta P_s + \gamma P_s^3) P_0 N^{-1}}{k_B T}\right) \quad (4)$$

where P_0 is the spontaneous saturation polarization, and N is the number of elementary dipoles per unit cell. Using the relationship $k_B T_C = \beta \cdot P_0^2 / N$ (where T_C is the Curie ferroelectric point) and designations of the normalized values $\sigma_s \equiv P_s / P_0$, $\tau \equiv T / T_C$, $g \equiv \gamma P_0^2 / \beta$, one can derive an expression that is convenient for analyzing the experimental data:

$$\sigma_s(T) = \tanh\left(\frac{\sigma_s(T) + g \sigma_s^3(T)}{\tau}\right) \quad (5)$$

where the parameter g is a quantitative criterion of the order of the transition to the ferroelectric state [61]. The analysis of the experimental dependences $P_s(T)$ using Expression (5) is shown in Figure 8.

The value $g \approx 0.48(3)$ in the temperature range $T_3 < T < T_2$ indicates a significant contribution of the quadrupolar interactions ($\gamma \neq 0$) in Expression (3), which, in turn, is a feature of the first-order transitions [61,62]. A similar behavior was observed for many oxide systems, in particular, those demonstrating multiferroic properties [63]. The transition point $T_C \approx 437$ K of the ferroelectric state, having been evaluated within the framework of this approach based on the description of $P_s(T)$, insignificantly differs from the temperature of the structural transition $Im \leftrightarrow I2/m$ ($T_2 \approx 442$ K) determined for the sample $\text{BiMn}_{6.96}\text{Fe}_{0.04}\text{O}_{12}$ from the thermodynamic data (Figure 2a). We suggest that the observed first-order transition at T_2 stems from an inevitable coupling between the electric polarization and the crystal lattice. There is a simultaneous structural change accompanying this transition as evidenced by the above finding. By using a simple phenomenological approach (see Appendix D), it can be shown that the coupling between spontaneous polarization (P_s) and strain (ϵ) can switch an otherwise second-order transition to a first-order transition. Moreover, there is a relationship between the strength of the ferroelastic coupling and the size of the hysteresis ~ 20 K (Figure 2a) of the resultant first-order transition. It is known that the size of hysteresis is determined by the energy barrier at T_C (Figure S4),

which is largely dependent on the magnitude of the ferroelastic coupling coefficient λ in the fourth-order term of the Landau free energy (see Equation A8). On the other hand, a larger λ also leads to a larger spontaneous lattice distortion upon the first-order phase transition. Therefore, the magnitude of thermal hysteresis increases with an increase in lattice distortion.

In the range $T_{N1} \leq T \leq T_3$, the dependence $P_s(T)$ demonstrates a kink at the point T_3 , and its course follows Expression (4) with the parameter $g \approx 0$, which, upon extrapolation to ~ 294 K (see Figure 8), should correspond to a “gradual” second-order phase transition [61]. A discussion of the nontrivial course of the dependencies $P_s(T)$ is beyond the scope of our work; however, it may motivate someone to study this unusual system using new independent local and macroscopic methods and theoretical approaches.

2.5. Mössbauer Study in the Temperature Range $T < T_{N1}$

The quadrupole doublets at temperatures slightly below the Néel point ($T < T_{N1} \approx 50$ K) contain the broadened components that reflect hyperfine magnetic fields B_{hf} induced on the ^{57}Fe nuclei (Figure 9a). The spectra were fitted via a reconstruction of distributions $p(B_{hf})$ characterized by a certain dispersion $D_p(\delta)$ at a given temperature. The kink on the temperature dependence $D_p(\delta) = f(T)$ (Figure 9b; Table S6 for data) corresponds to the temperature 57(3) K, which, within the measurement error, coincides with $T_{N1} \approx 59$ K for undoped manganite $\text{BiMn}_7\text{O}_{12}$ (Figure 2b). This result gives independent confirmation of the stabilization of ^{57}Fe probes in the lattice of the $\text{BiMn}_7\text{O}_{12}$ manganite under study.

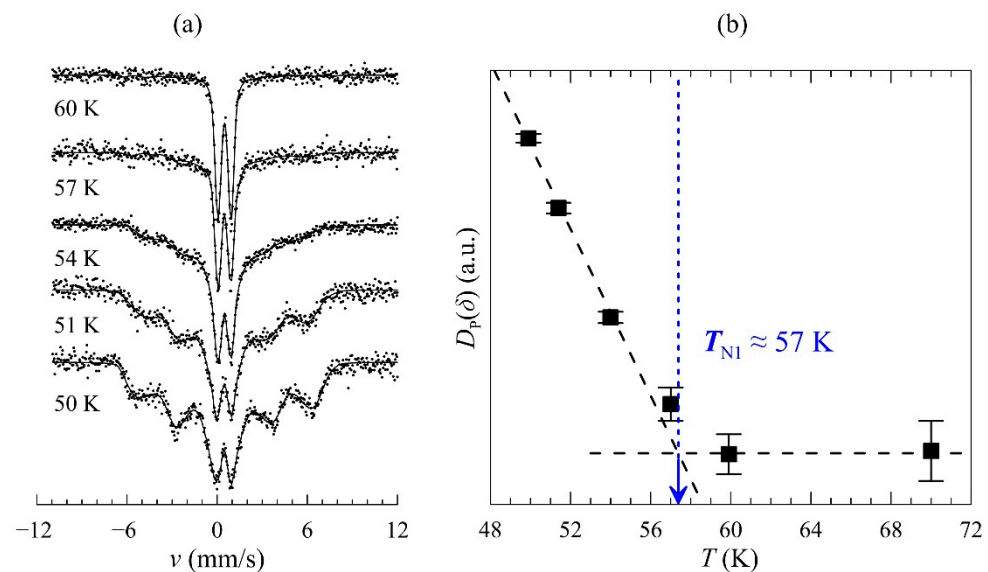


Figure 9. (a) ^{57}Fe Mössbauer spectra of $\text{BiMn}_{6.96}\text{Fe}_{0.04}\text{O}_{12}$ near T_{N1} fitted as the distributions of the single Lorentz line; (b) the temperature dependence of the dispersion $D_p(\delta)$ of the isomer shift δ . The kink was used to evaluate the magnetic phase transition point (see text).

At low temperatures, $T \ll T_{N1}$, the Mössbauer spectrum of $\text{BiMn}_{6.96}\text{Fe}_{0.04}\text{O}_{12}$ has an asymmetric and slightly broadened Zeeman structure (Figure 10), which can be described by a superposition of four unequally broadened sextets in accordance with the structural data for the triclinic phase $\text{BiMn}_7\text{O}_{12}$ [4]. With increasing temperature, the profiles of these sextets change noticeably, which is characteristic of the system exhibiting relaxation processes. Earlier studies showed [64] that this behavior could be attributed to the magnetic excitation of paramagnetic impurity ions within magnetically ordered matrices, where competing exchange interactions play a significant role. When embedded within the manganite matrix, impurity cations Fe^{3+} with half-filled orbitals are surrounded by the JT Mn^{3+} cations with anisotropic orbital occupation. This can lead to a noticeable weakening of the exchange interactions between the impurity cations and their magnetic environment. Essentially, this suggests that iron cations can undergo lower-energy magnetic excitations,

influencing also the neighboring Mn^{3+} cations rather than only Fe^{3+} cations. An increase in temperature leads to the progressive occupation of magnetic Fe^{3+} states characterized by different projections (S_Z) of the total spin $S = 5/2$. As the magnetic interaction of iron with its surroundings is weakened, the relaxation of spin between the states $|5/2, S_Z\rangle$ decelerates. If the relaxation period τ_R closely corresponds to the period of Larmor precession (τ_L) of the ^{57}Fe nuclear spin around the hyperfine field B_{hf} , the Mössbauer spectra typically have complex relaxation profiles [65].

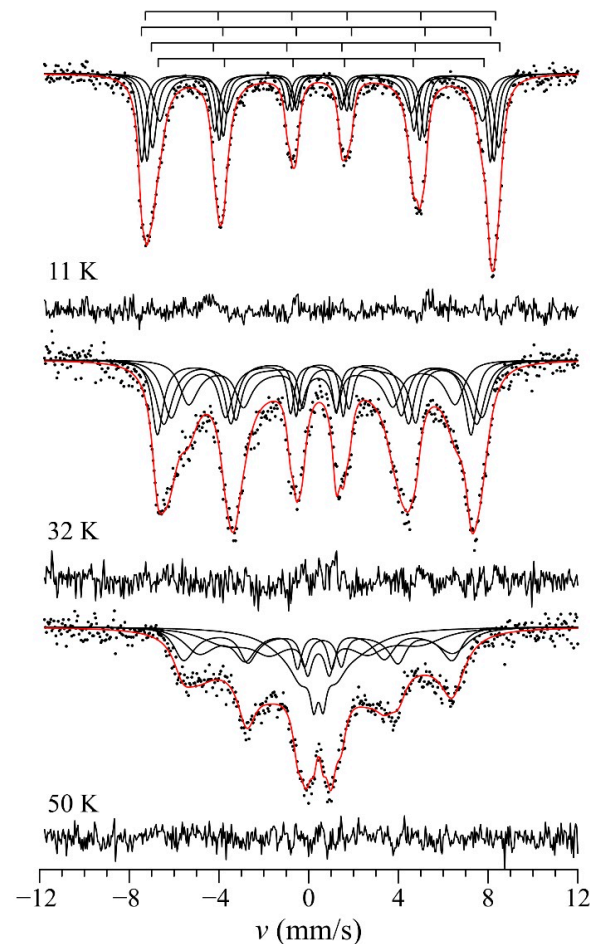


Figure 10. ^{57}Fe Mössbauer spectra of $\text{BiMn}_{6.96}\text{Fe}_{0.04}\text{O}_{12}$ at $T < T_{\text{N1}}$, fitted with the multilevel magnetic spin relaxation (see text). Black curves are subspectra obtained during fitting procedure, red curves are summarized fitted spectra. The differences between experimental and fitted data are also shown in the bottom of each spectrum.

Additionally, it should be noted that the SEM data indicates that an average particle size exceeded $\sim 2 \mu\text{m}$ for the $\text{BiMn}_{6.96}\text{Fe}_{0.04}\text{O}_{12}$ sample (Figure S3). Consequently, the observed relaxation behavior of the Mössbauer spectra cannot be attributed to the superparamagnetic or superferromagnetic states of small particles [65,66].

Taking into account the considerations presented above, the spectra were fitted using a multilevel relaxation model [67]. This model is based on the assumption that in the effective magnetic Weiss field, spin $S = 5/2$ of the Fe^{3+} cation, stochastically relaxes between Zeeman states $|5/2, S_Z\rangle$ [67]. Along with the static parameters (δ , eQV_{ZZ} and B_{hf}), the model includes variable relaxation parameters, namely, the relaxation frequency $\Omega_R (=1/\tau_R)$ and the relative population (s) of the Zeeman sublevels between which the relaxation occurs. A detailed description of this model can be found in [67]. This allowed us to process the whole series of spectra measured in the temperature range $10 \text{ K} < T < T_{\text{N1}}$. It should be noted that the static and relaxation parameters of the Mössbauer spectra remain virtually

unchanged, which indicates the stability of a complex model of spectrum processing. A smooth and continuous change in the hyperfine magnetic field near T_{N1} indicates the occurrence of a second-order magnetic phase transition. This conclusion is consistent with the results of a theoretical study of undoped manganite $\text{BiMn}_7\text{O}_{12}$, according to which the transition at $T_{N1} = 59$ K corresponds to the formation of a single E -type AFM structure [68]. At the same time, the magnetic phase transitions at $T_{N2} \approx 50$ K and $T_{N3} \approx 24$ K cannot be seen in the Mössbauer spectra because the former does not change the local magnetic environment of manganese (probe iron) cations in B sites, and the second transition (T_{N3}) leads to the magnetic ordering of Mn^{3+} in the A'' sublattice.

Characteristic of spin–spin relaxation, there are no obvious changes in the frequency Ω_R as a function of temperature. However, the values of $\Omega_R \sim (0.2\text{--}0.5) \times 10^9 \text{ s}^{-1}$ are found to be significantly lower than the characteristic frequencies of spin waves $\Omega_S \approx k_B T / \hbar = 10^{11}\text{--}10^{12} \text{ s}^{-1}$ ($T = 1\text{--}100$ K) in conventional magnetic systems [65]. This indicates that the spin fluctuations involving iron probes are predominantly local. Furthermore, the Ω_R value is comparable to the Larmor frequency $\Omega_R \approx 10^8 \text{ s}^{-1}$ of the ^{57}Fe nuclear spin in the hyperfine magnetic field $\langle B_{\text{hf}} \rangle \approx 50$ T, thus supporting our assumption about the relaxed nature of the observed spectra.

Figure 11 shows the temperature dependence of the hyperfine field $\langle B_{\text{hf}}(T) \rangle$ averaged over all partial spectra $\text{Fe}(i)$, which was approximated for spin $S = 5/2$ using the parametric Brillouin function:

$$\langle B_{\text{hf}}(T) \rangle = \langle B_{\text{hf}}(0) \rangle B_{5/2} \left[\xi \frac{5}{2} \left(\frac{T_N}{T} \right) \sigma_{\text{Mn}}(T) \right] \quad (6)$$

where $\xi = J_{\text{FeMn}}/J_{\text{MnMn}}$ is the ratio of exchange integrals that characterize the magnetic interactions of Fe^{3+} probes with the surrounding manganese cations (J_{FeMn}) and the averaged interactions between the Mn^{3+} cations themselves (J_{MnMn}). The value $\xi = 0.67(3)$ obtained from the best fit of the experimental spectra evidences the weakening of the exchanged magnetic interactions of the iron cations with the manganese sublattice, which is equivalent to decreasing the effective Weiss field [69]. This can result from a so-called “orbital dilution”, a phenomenon characteristic of the impurity cations of transition metals with non-degenerate orbital electron states (Fe^{3+} , $\text{Cr}^{3+} \dots : \langle L \rangle = 0$, where L is the total orbital momentum) if they are stabilized within the matrix of transition metals with degenerate orbital states (Rh^{4+} , $\text{Mn}^{3+} \dots : \langle L \rangle \neq 0$) [70,71]. It was shown previously that such impurity centers behave as peculiar “orbital defects” due to the absence of orbital degeneration, i.e., orbital degrees of freedom. Even at very low concentrations, they can significantly affect the magnetic structure of the compound. Experimental methods employed to study such systems are currently in their early stages of development.

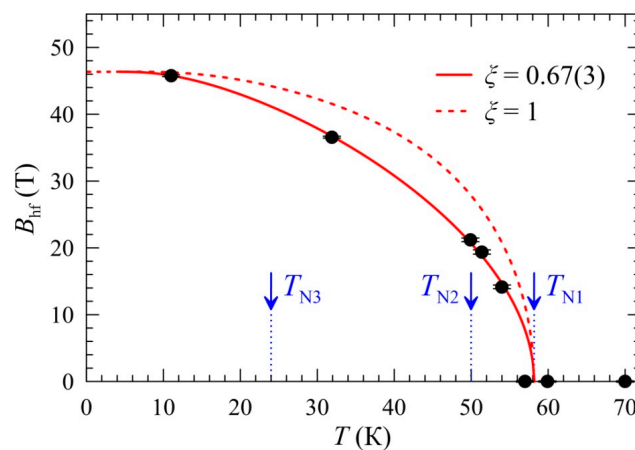


Figure 11. The temperature dependence $B_{\text{hf}}(T)$ of the hyperfine magnetic field B_{hf} at ^{57}Fe nuclei approximated using a modified Brillouin function (see text). The dashed red line shows the “pure” Brillouin law for spin $S = 5/2$. Black dots are experimental mean values of the hyperfine fields.

3. Materials and Methods

The manganite $\text{BiMn}_{6.96}\text{Fe}_{0.04}\text{O}_{12}$ was synthesized in a high-pressure, “belt”-type chamber. A stoichiometric mixture of Mn_2O_3 (99.9%, Rare Metallic Co., Tokyo, Japan) Bi_2O_3 (99.9999%, Rare Metallic Co., Tokyo, Japan), and $^{57}\text{Fe}_2\text{O}_3$ (95.5% enriched with ^{57}Fe , Trace Sciences International, Richmond Hill, ON, Canada) was filled into a gold capsule in which it was subjected to a pressure of ~6 GPa followed by heating to 1323 K for 10 min. The sample was quenched to room temperature after holding for 120 min. The synthesis of undoped manganite $\text{BiMn}_7\text{O}_{12}$ is described in more detail in [3].

The X-ray diffraction data were acquired using a synchrotron source of X-rays (SXRPD) in a large Debye–Sherrer chamber with the line BL15XU (SPring-8, Sayo, Japan) and the 2θ value ranging from 3° to 60° with a step of 0.003° . The monochromatic radiation with the wavelength of $\lambda = 0.65298 \text{ \AA}$ was used. Experiments were performed in a temperature range of between 100 and 670 K. Prior to measuring, the powder samples were tightly packed in a Lindemann glass capillary (for the 100–400 K range) and a quartz capillary (for the 350–670 K range) with an internal diameter of 0.1 mm. The capillaries were cooled using an N_2 flow when the low-temperature measurements were performed. The processing of the diffraction patterns and refinement of the crystal lattice parameters were performed using the Rietveld method, using the RIETAN-2000 software similar to the procedure described in [3].

Scanning electron microscopy (SEM) images were taken on a NVision 40 electron microscope (Carl Zeiss; Oberkochen, Germany) equipped with an Oxford Instruments X-Max analyzer. The accelerating voltage varied in the range from 3 to 20 kV.

For measuring differential scanning calorimetry (DSC) curves on a Mettler Toledo DSC1 STAR^c calorimeter in the temperature range 125–673 K, samples were placed in Al crucibles, the rate of heating/cooling in the nitrogen flow being 10 K/min.

The heat capacity measurements were carried out on a PPMS calorimeter (Quantum Design, San Diego, CA, USA) in the temperature range of 2–300 K in the modes of heating and cooling in external magnetic fields ranging from 0 to 90 kOe.

Magnetic susceptibility was measured on a SQUID MPMS 1T magnetometer (Quantum Design, San Diego, CA, USA) in the temperature range of 2–350 K in the ZFC (cooling without external magnetic field) and FC (cooling in the external magnetic field 10 kOe in strength) modes.

Mössbauer spectra were measured with a conventional electrodynamic-type spectrometer in the constant acceleration mode with a 1450 MBq $^{57}\text{Co}(\text{Rh})$ γ -ray source. The values of the isomer shift are given relative to $\alpha\text{-Fe}$ (298 K). Processing of the experimental spectra was performed with the use of the program package “SpectrRelax” [72]. Computations of the EFG parameters were carried out using the “GradientNCMS” software (ver. 8.3) designed by the authors and are represented in more detail in [73].

4. Conclusions

We explored the interplay between the local crystal structure of the multiferroic $\text{BiMn}_7\text{O}_{12}$ manganite and the processes of its spontaneous polarization and magnetic ordering using ^{57}Fe -probe Mössbauer spectroscopy. It was shown that Fe^{3+} probes statistically substitute isovalent Mn^{3+} cations in the octahedral oxygen local environment. The parameters of the electric hyperfine interactions of ^{57}Fe nuclei reflect the symmetry of the crystalline environment of Mn^{3+} cations in these sites.

The calculations of the EFG parameters, considering both monopole and dipole contributions, are in accordance with our experimental results, demonstrating that, in the paraelectric phase (at $T > T_2$), cations Bi^{3+} , even while existing in locally distorted crystalline environments, maintain their electrical dipole moments p_{Bi} , which are randomly oriented within the cubic lattice. As a result, the phase transitions into the ferroelectric state involve the ordering of p_{Bi} dipoles, i.e., they may be considered the transitions of the “order-disorder” type.

It was determined that the monotonous decrease in $\Delta(T)$ from T_2 up to T_1 can indicate a gradual increase in the symmetry of $(\text{Fe}^{3+}\text{O}_6)$ polyhedra while approaching the temperature of the structural transition $Im\bar{3} \rightarrow I2/m$, which is corroborated by the synchrotron diffraction studies of undoped $\text{BiMn}_7\text{O}_{12}$. This characteristic behavior has been independently registered through methods that are entirely different in their physical nature. Thus, it strongly indicates the occurrence of the second-order JT phase transition. Its mechanism can be classified as a structural transition of the “displacive” type, in contrast to “order-disorder” transitions.

Using the Born model, we calculated dynamic ion charges that indicate only a minor ion polarization and the predominance of ionic contributions in the spontaneous electrical polarization of the crystal. The observed robust temperature dependence of the quadrupole splitting $\Delta_i(T)$ of the partial spectra Fe(i) is governed by the temperature dependence $P_s(T)$. The dependence $P_s(T)$ on the opposite sides of the phase transition $P1 \leftrightarrow Im$ ($T_3 \approx 240$ K) significantly differs in its behavior. In the range $T_3 < T < T_2$, $P_s(T)$ indicates that the ferroelectric–paraelectric phase transition is of the first order. The Curie point $T_C \approx 437$ K determined from the Mössbauer data closely coincides with the temperature of the structural transition $Im \leftrightarrow I2/m$. The proposed algorithm for finding the correlation between the experimental dependencies $\Delta_i(T)$ for the probe ^{57}Fe nuclei and the polarization $P_s(T)$ of the crystal can be applied to other systems with ferroelectric and multiferroic properties.

At low temperatures, $T < T_{N1}$, and the ^{57}Fe Mössbauer spectra demonstrate relaxation behavior. This can result from a so-called “orbital dilution” characteristic of the impurity cations of transition metals with non-degenerate orbital electron states within the matrix of transition metals with degenerate orbital states.

Supplementary Materials: The supporting information can be downloaded at: <https://www.mdpi.com/article/10.3390/ijms25031437/s1>.

Author Contributions: Conceptualization, A.V.S., A.A.B. and I.A.P.; methodology, I.S.S., V.I.N. and A.V.S.; software, A.V.S.; validation, I.S.S. and A.A.B.; formal analysis, I.S.S. and V.I.N.; investigation, I.S.S., V.I.N., M.N.S. and A.A.B.; data curation, I.S.S., V.I.N., A.V.S. and A.A.B.; writing—original draft preparation, A.V.S. and I.A.P.; writing—review and editing, A.V.S., A.A.B. and I.A.P.; visualization, I.S.S. and I.A.P.; supervision, A.V.S. and I.A.P.; project administration, A.V.S. and I.A.P.; funding acquisition, I.S.S. All authors have read and agreed to the published version of the manuscript.

Funding: This research was funded by the Russian Science Foundation (RSF, grant No. 19-73-10034). The synchrotron radiation experiments were conducted at the former NIMS beamline (BL15XU) of SPring-8 with the approval of the former NIMS Synchrotron X-ray Station (proposal number: 2017B4502).

Institutional Review Board Statement: Not applicable.

Informed Consent Statement: Not applicable.

Data Availability Statement: The data presented in this study are available on request from the corresponding author.

Acknowledgments: We thank Y. Katsuya and M. Tanaka for their help at SPring-8.

Conflicts of Interest: The authors declare no conflicts of interest. The funders had no role in the design of the study; in the collection, analyses, or interpretation of data; in the writing of the manuscript; or in the decision to publish the results.

Appendix A

Electric Field Gradient Calculation Details

In terms of an ionic approximation, i.e., without regard for the covalence of the chemical bonds between the anionic and cationic sublattices, the EFG lattice tensor components on ^{57}Fe nuclei represent the sum of the monopole (V^{mon}) and dipole (V^{dip}) contributions [74]

$$V_{ij}^{lat} = V_{ij}^{mon} + V_{ij}^{dip} = (1 - \gamma_{\infty}) \sum_k \frac{\partial^2}{\partial x_i \partial x_j} \left[\frac{q_k}{r_k} + \frac{r_{ik} p_{ik}}{r_k^3} \right] \quad (A1)$$

where γ_{∞} is the Sternheimer antishielding factor, q_k is the effective charge of the k th ion in the lattice, r_k is the distance between the k th ion and the ^{57}Fe nucleus, and r_{ik} is the projection of the radius vector r_k on the direction of the i th projection of the electric dipole moment of the k th ion p_{ik} (where $i = x, y, z$). The dipole moments of the ions (p_k) and their projections (p_{ik}) were assumed to be calculated in terms of the Born model [59]: $p_k = Z_k \Delta p_k$ or $p_{ik} = Z_k \Delta x_{ik}$, where Z_k is the Born charge of the k th ion, which was taken to be an isotropic scalar quantity, and Δp_k (Δx_{ik}) is the displacement vector of the k th ion (and its i th projection) from its centrosymmetrical position. Δp_k and Δx_{ik} were calculated using the crystallographic data for the $\text{BiMn}_7\text{O}_{12}$ manganite obtained at 300 K [3]. To estimate the Born charges, we used the following procedure: charges Z_{Bi} , Z_{Mn} , and Z_{O} , and the corresponding dipole moments p_{ik} were sequentially varied at displacement Δx_{ik} until the best agreement with the experimental quadrupole splittings Δ_i . At the first stage of this procedure, the desired Born charges of the ions Z_k were taken to be equal to their formal oxidation levels in the $\text{BiMn}_7\text{O}_{12}$ compound. As a result, we obtained the values $Z_{\text{Bi}} = +3.30$, $Z_{\text{Mn1}} \approx Z_{\text{Mn2}} = +3.30$, and $Z_{\text{O}} = -2.20$, which fall within the Born charge range obtained for the corresponding ions in other perovskite-like oxides [60]. Using the projections of the electric dipole moments p_{ik} , we can calculate the spontaneous polarization of the manganite,

$$P_s = \frac{1}{V} \left(\sum_i \left(\sum_k p_{ik} \right)^2 \right)^{\frac{1}{2}} \quad (A2)$$

The value obtained at $T = 300$ K ($P_s(T_0) \sim 9 \mu\text{C}/\text{cm}^2$) agrees with the value ($7 \mu\text{C}/\text{cm}^2$ at 300 K) obtained earlier for ^{57}Fe -free manganite $\text{BiMn}_7\text{O}_{12}$ (space group Im) [3]. All these results demonstrate that, despite the initial assumptions, the proposed calculation scheme is quite self-consistent and can be extended to the temperature range for which structural data are absent.

The Born charges obtained for Bi^{3+} , Mn^{3+} , and O^{2-} ions (Z_i) can be compared to the effective charges (S) calculated using the Brown model by using the data on the crystal structure of the plain $\text{BiMn}_7\text{O}_{12}$ manganite [3].

$$S = \sum_k s_k = \sum_k \exp\left(\frac{r_0 - r_k}{B}\right) \quad (A3)$$

where r_k is the metal–oxygen distance for the k th pair $M^{3+}\text{-O}^{2-}$ (where $M = \text{Bi}, \text{Mn}$), r_0 is a constant for the given metal grade ($r_0 = 2.09$ for $\text{Bi}^{3+}\text{-O}^{2-}$ and $r_0 = 1.760$ for $\text{Mn}^{3+}\text{-O}^{2-}$), and $B = 0.37$ [75]. Using this equation, we calculated the effective charges S of the Bi^{3+} , Mn^{3+} , and O^{2-} ions occupying nonequivalent crystallographic positions for each of the two structural modifications of $\text{BiMn}_7\text{O}_{12}$.

Charges $\langle S_{\text{Bi}} \rangle$, $\langle S_{\text{Mn}} \rangle$, and $\langle S_{\text{O}} \rangle$ that were averaged for each kind of ions are presented in the Table S1. As would be expected, the obtained values of $\langle S \rangle$ are very close to the formal oxidation levels of the corresponding atoms but are lower than their Born charges. The high Born charges, which are several times higher than the formal oxidation levels for most perovskite-like metal oxides, are associated with the deformation (polarizability) of the electron shell of an ion when it is displaced from the centrosymmetrical position in a crystal [59]. However, in our case, the discrepancy between the Born (Z) and effective ($\langle S \rangle$) charges is not so significant (Table S1), which indirectly confirms the validity of the ion model used in this work.

The temperature dependences of the dipole moment $p_k(T)$ and the related spontaneous polarization $P_s(T)$, which are likely to be the main cause of the sharp temperature-induced change in the splitting $\Delta_1(T)$ and $\Delta_2(T)$, were taken into account using the approximate expressions $p_k(T) = \zeta_k(T)p_k(T_0)$ and $P_s(T) = \zeta_k(T)P_k(T_0)$, in which $p_k(T_0)$ and $P_k(T_0)$ are the

known values of the corresponding parameters at a given temperature $T_0 = 300$ K. Our preliminary calculations showed that the same type of functions $\zeta_k(T) \equiv \zeta_k(T_0)$,

$$\zeta(T) = \frac{p_{\text{Bi}}(T)}{p_{\text{Bi}}(T_0)} = \frac{p_{\text{Mn}(i)}(T)}{p_{\text{Mn}(i)}(T_0)} = \frac{p_{\text{O}(i)}(T)}{p_{\text{O}(i)}(T_0)} = \frac{p_{\text{S}}(T)}{p_{\text{S}}(T_0)} \quad (\text{A4})$$

can be taken for all ions in order to achieve agreement with the experiment data and to decrease the number of variable parameters.

Appendix B

Distortion Parameters Calculation Details

To calculate the distortion (Δ_d) parameters of MnO_6 polyhedra, we used this equation:

$$\Delta_d = \frac{1}{6} \sum_{n=1}^6 \left[\frac{l_n - \frac{1}{6} \left(\sum_{n=1}^6 l_n \right)}{\frac{1}{6} \left(\sum_{n=1}^6 l_n \right)} \right]^2 = \frac{1}{6} \sum_{n=1}^6 \left[\frac{l_n - l_{\text{med}}}{l_{\text{med}}} \right]^2 \quad (\text{A5})$$

where l_n is the length of the n th Mn-O_(n) bond and l_{med} is the average value of the corresponding bonds in MnO_6 .

Appendix C

Electric Field Gradient Calculation within P1 pseudocell ($T > T_1$) Details

In the general case the sublattice A' cations in quadrupole perovskites (which are Bi^{3+} cations in the perovskite $\text{BiMn}_7\text{O}_{12}$) are located in the partial position $2a$ with coordinates (0, 0, 0). However, as noted in [3], the presence of a stereochemically active lone-pair $6s^2$ electrons directed towards the center of the oxygen dodecahedron $\text{Bi}^{3+}\text{O}_{12}$ leads to a displacement of the Bi^{3+} cation itself along the diagonal from its partial position $2a$ to the new partial position $16f$ with coordinates ($\pm 0.0223(9)$, $\pm 0.0223(9)$, $\pm 0.0223(9)$).

To account for the influence of the Bi^{3+} cations displacement to the new partial position $16f$, the calculations were carried out within the framework of a pseudocell. The initial crystal lattice was increased by a factor of 8 to the size of a cube with a decrease in the symmetry of the lattice to the space group $P1$ with parameters ($a_{P1} = b_{P1} = c_{P1} = 2a_{\text{ini}} = 14.96716 \text{ \AA}$) and initial cubic angles, while maintaining the coordinates of other types of atoms, however, the coordinates of the Bi^{3+} cations were chosen randomly from 8 available triple of coordinates for each position with consideration that $\text{BiMn}_7\text{O}_{12}$ is paraelectric at $T > T_1$. The calculations were carried out on each of the 64 manganese atoms of the pseudocell due to the environment nonequivalence of each of them. Thus, a set of 64 quadruple distribution splittings Δ was used, from which, using methods of mathematical statistics, the average values of the quadruple splitting Δ_{av} and the quadruple splitting dispersion D were calculated.

Appendix D

Extension of the Landau Theory to First-Order Phase Transitions

For a ferroelectric system with two order parameters of electrical polarization P_z (primary) and strain ε (secondary), generic Landau free energy (F) can be expressed as [76]:

$$F(P_z, \varepsilon) = \frac{1}{2} a(T) P_z^2 + \frac{1}{4} b P_z^4 + \frac{1}{6} c P_z^6 + \frac{1}{2} k \varepsilon^2 + \lambda \varepsilon \cdot P_z^2 \quad (\text{A6})$$

This equation consists of three contributions: (i) the electric energy due to the primary order parameter P_z : $\frac{1}{2} a(T) P_z^2 + \frac{1}{4} b P_z^4 + \frac{1}{6} c P_z^6$, where the coefficient $a(T)$ is assumed to be temperature dependent $a(T) = a_0(T - T_C)$. Usually, it is assumed that the system intrinsically tends to undergo a second-order transition and, thus, the coefficient b (>0)

of the fourth-order term is positive; c is the coefficient of the sixth-order term, and $c > 0$. (ii) The elastic energy due to the second-order parameter ε : $\frac{1}{2}k\varepsilon^2$, where k is the elastic modulus and, thus, $k > 0$. (iii) The ferroelastic coupling energy is as follows: $\lambda\varepsilon \cdot P_z^2$, where λ is the coupling coefficient.

Minimizing the total energy with respect to the strain, $\partial F/\partial\varepsilon = 0$, yields a relation between primary and secondary parameters P_z and ε , respectively,

$$\varepsilon = -\frac{\lambda}{k}P_z^2 \quad (\text{A7})$$

Substituting Equation (A7) into Equation (1), we obtain a renormalized Landau free energy,

$$F'(P_z) = \frac{1}{2}a(T)P_z^2 + \frac{1}{4}\left(b - \frac{2\lambda^2}{k}\right)P_z^4 + \frac{1}{6}cP_z^6 = \frac{1}{2}a(T)P_z^2 + \frac{1}{4}b'P_z^4 + \frac{1}{6}cP_z^6 \quad (\text{A8})$$

The most important consequence of the ferroelastic coupling is that the coefficient ($b > 0$) of the fourth-order term is renormalized and now becomes $b' \equiv (b - 2\lambda^2/k)$. As the coefficient b is usually a small positive constant and elastic modulus is always positive ($k > 0$), a coupling coefficient λ of certain magnitude can make $b' < 0$. Because a negative fourth-order term in Landau free energy (Equation (A8)) creates an energy barrier in the free energy landscape, this leads to a first-order transition. It is interesting that a renormalization group approach also yields a similar conclusion: a second-order transition is changed into a first-order transition if a primary order parameter (P_z) is coupled to the strain in the fluctuation region near T_C [77].

Minimizing $F'(P_z)$ with respect to the polarization P_z , $\partial F'/\partial P_z = 0$, provides the following description, summarized in Figure S6 for the paraelectric-ferroelectric transition. For $T > T^{**} = T_C + (b')^2/4a_0c$, the paraelectric phase ($P_z = 0$) is the only stable phase. At $T \approx T^{**}$ ferroelectric phase ($P_z \neq 0$), corresponding to

$$P_z(T) = \pm \left[\frac{-b' + \left(\frac{1}{4}(b')^2 - a_0c(T - T_C)\right)^{1/2}}{c} \right]^{1/2} \quad (\text{A9})$$

arises as a metastable state, associated with a secondary minimum in the non-equilibrium curve $F'(T, P_z)$. On cooling, the stability increases and paraelectric and ferroelectric phases become equally stable at $T^* = T_C + 3(b')^2/16a_0c$. Below T^* paraelectric phase, metastable decreases to T_C , where it becomes unstable. A region of coexistence between paraelectric and ferroelectric phases in the temperature interval $\Delta T = 1/16(b')^2/a_0c$, in which the two phases are alternately metastable. The phase transition may occur at any temperature within the ΔT interval. However, the most probable transition temperature is T_C , corresponding to an equal stability for the two phases. The existence of a region of coexistence for the two phases implies a thermal hysteresis on cycling across the paraelectric-ferroelectric transition.

The obtained Equation (A8) allows for an important prediction about the relationship between the strength of the ferroelastic coupling and the size of the hysteresis of the resulting first-order phase transition. The size of the hysteresis is determined by the energy barrier at T_C (Figure S6), which is largely dependent on the magnitude of the negative fourth-order term $\frac{1}{4}b'P_z^4$ [6,8]. The more negative this term is, the larger the transition barrier and the thermal hysteresis. A large ferroelastic coupling coefficient λ contributes to a large negative fourth-order term $\frac{1}{4}b'P_z^4$ and, thus, contributes to a larger transition hysteresis. On the other hand, from Equation (A7), one can see that a larger ferroelastic coupling coefficient λ also leads to a larger spontaneous lattice distortion upon the first-order ferroelectric transition. Therefore, the strength of the coupling coefficient λ can be represented by the magnitude of the spontaneous lattice distortion. As a result, Equation (A8) predicts that the magnitude of thermal hysteresis increases with an increase in lattice distortion.

References

1. Mezzadri, F.; Calestani, G.; Calicchio, M.; Gilioli, E.; Bolzoni, F.; Cabassi, R.; Marezio, M.; Migliori, A. Synthesis and characterization of multiferroic BiMn₇O₁₂. *Phys. Rev. B* **2009**, *79*, 100106. [\[CrossRef\]](#)
2. Gauzzi, A.; Rouse, G.; Mezzadri, F.; Calestani, G.L.; André, G.; Bourée, F.; Calicchio, M.; Gilioli, E.; Cabassi, R.; Bolzoni, F.; et al. Magnetolectric coupling driven by inverse magnetostriction in multiferroic BiMn₃Mn₄O₁₂. *J. Appl. Phys.* **2013**, *113*, 043920. [\[CrossRef\]](#)
3. Belik, A.A.; Matsushita, Y.; Kumagai, Y.; Katsuya, Y.; Tanaka, M.; Stefanovich, S.Y.; Lazoryak, B.I.; Oba, F.; Yamaura, K. Complex Structural Behavior of BiMn₇O₁₂ Quadruple Perovskite. *Inorg. Chem.* **2017**, *56*, 12272–12281. [\[CrossRef\]](#)
4. Sławiński, W.A.; Okamoto, H.; Fjellwåg, H. Triclinic crystal structure distortion of multiferroic BiMn₇O₁₂. *Acta Cryst.* **2017**, *73*, 313–320. [\[CrossRef\]](#)
5. Belik, A.A.; Matsushita, Y.; Khalyavin, D.D. Reentrant Structural Transitions and Collapse of Charge and Orbital Orders in Quadruple Perovskites. *Angew. Chem. Int. Ed.* **2017**, *56*, 10423–10427. [\[CrossRef\]](#)
6. Khalyavin, D.D.; Johnson, R.D.; Orlandi, F.; Radaelli, P.G.; Manuel, P.; Belik, A.A. Emergent helical texture of electric dipoles. *Science* **2020**, *369*, 680–684. [\[CrossRef\]](#)
7. Khomskii, D.I. *Transition Metal Compounds*; Cambridge University Press: Cambridge, UK, 2014.
8. Streltsov, S.V.; Khomskii, D.I. Orbital physics in transition metal compounds: New trends. *Physics-Uspekh* **2017**, *60*, 1121–1146. [\[CrossRef\]](#)
9. Sobolev, A.V.; Rusakov, V.S.; Gapochka, A.M.; Glazkova, I.S.; Gubaidulina, T.V.; Matsnev, M.E.; Belik, A.A.; Presniakov, I.A. ⁵⁷Fe Mössbauer spectroscopy study of cycloidal spin arrangements and magnetic transitions in BiFe_{1-x}Co_xO₃. *Phys. Rev. B* **2020**, *101*, 224409. [\[CrossRef\]](#)
10. Sobolev, A.V.; Bokov, A.V.; Yi, W.; Belik, A.A.; Presniakov, I.A.; Glazkova, I.S. Electric Hyperfine Interactions of ⁵⁷Fe Impurity Atoms in ACrO₃ Perovskite-Type Chromites (A = Sc, In, Tl, Bi). *J. Exp. Theor. Phys.* **2019**, *129*, 896–902. [\[CrossRef\]](#)
11. Goodenough, J.B. Theory of the Role of Covalence in the Perovskite-Type Manganites [La, M(II)]MnO₃. *Phys. Rev.* **1955**, *100*, 564–573. [\[CrossRef\]](#)
12. Radaelli, P.G.; Cox, D.E.; Marezio, M.; Cheong, S.-W. Charge, orbital, and magnetic ordering in La_{0.5}Ca_{0.5}MnO₃. *Phys. Rev. B* **1997**, *55*, 3015–3023. [\[CrossRef\]](#)
13. Khomskii, D. Classifying multiferroics: Mechanisms and effects. *Physics* **2009**, *2*, 20. [\[CrossRef\]](#)
14. Kouřil, K.; Chlan, V.; Štěpánková, H.; Řezníček, R.; Laguta, V.V.; Raevski, I.P. NMR Study of Multiferroic Iron Niobate Perovskites. *Acta Phys. Pol. A* **2015**, *127*, 234–236. [\[CrossRef\]](#)
15. Ivanov, Y.N.; Sukhovskii, A.A.; Volkov, N.V. ¹¹B NMR study of Ho_{1-x}Y_xAl₃(BO₃)₄ multiferroics. *J. Struct. Chem.* **2013**, *54* (Suppl. S1), S130–S136. [\[CrossRef\]](#)
16. Smol'nikov, A.G.; Ogloblichev, V.V.; Verkhovskii, S.V.; Mikhalev, K.N.; Yakubovskii, A.Y.; Kumagai, K.; Furukawa, Y.; Sadykov, A.F.; Piskunov, Y.V.; Gerashchenko, A.P.; et al. ⁵³Cr NMR Study of CuCrO₂ Multiferroic. *JETP Lett.* **2015**, *102*, 674–677. [\[CrossRef\]](#)
17. Prinz-Zwick, M.; Gimpel, T.; Geirhos, K.; Ghara, S.; Steinbrecht, C.; Tsurkan, V.; Büttgen, N.; Kézsmárki, I. Probing multiferroic order parameters and domain population via nuclear spins. *Phys. Rev. B* **2022**, *105*, 014301. [\[CrossRef\]](#)
18. Smol'nikov, A.G.; Ogloblichev, V.V.; Germov, A.Y.; Mikhalev, K.N.; Sadykov, A.F.; Piskunov, Y.V.; Gerashchenko, A.P.; Yakubovskii, A.Y.; Muflikhonova, M.A.; Barilo, S.N.; et al. Charge Distribution and Hyperfine Interactions in the CuFeO₂ Multiferroic According to ^{63,65}Cu NMR Data. *JETP Lett.* **2018**, *107*, 134–138. [\[CrossRef\]](#)
19. Zalessky, A.V.; Frolov, A.A.; Khimich, T.A.; Bush, A.A.; Pokatilov, V.S.; Zvezdin, A.K. ⁵⁷Fe NMR study of spin-modulated magnetic structure in BiFeO₃. *EPL* **2000**, *50*, 547–551. [\[CrossRef\]](#)
20. Baek, S.-H.; Reyes, A.P.; Hoch, M.J.R.; Moulton, W.G.; Kuhns, P.L.; Harter, A.G.; Hur, N.; Cheong, S.-W. ⁵⁵Mn NMR investigation of the correlation between antiferromagnetism and ferroelectricity in TbMn₂O₅. *Phys. Rev. B* **2006**, *74*, 140410. [\[CrossRef\]](#)
21. Jo, E.; Park, S.; Lee, J.; Lee, S.; Shim, J.H.; Suzuki, T.; Katsufuji, T. Orbital reorientation in MnV₂O₄ observed by V NMR. *Sci. Rep.* **2017**, *7*, 2178. [\[CrossRef\]](#) [\[PubMed\]](#)
22. Smol'nikov, A.G.; Ogloblichev, V.V.; Verkhovskii, S.V.; Mikhalev, K.N.; Yakubovskii, A.Y.; Furukawa, Y.; Piskunov, Y.V.; Sadykov, A.F.; Barilo, S.N.; Shiryayev, S.V. Specific Features of Magnetic Order in a Multiferroic Compound CuCrO₂ Determined Using NMR and NQR Data for ^{63,65}Cu Nuclei. *Phys. Met. Metallogr.* **2017**, *118*, 134–142. [\[CrossRef\]](#)
23. Pregelj, M.; Jeglič, P.; Zorko, A.; Zaharko, O.; Apih, T.; Gradišek, A.; Komelj, M.; Berger, H.; Arčon, D. Evolution of magnetic and crystal structures in the multiferroic FeTe₂O₅Br. *Phys. Rev. B* **2013**, *87*, 144408. [\[CrossRef\]](#)
24. Kalvius, G.M.; Litterst, F.J.; Hartmann, O.; Wäppling, R.; Krimmel, A.; Mukhin, A.A.; Balbashov, A.M.; Loidl, A. Magnetic properties of the multiferroic compounds Eu_{1-x}Y_xMnO₃ (x = 0.2 and 0.3). *J. Phys. Conf. Ser.* **2014**, *551*, 012014. [\[CrossRef\]](#)
25. Baker, P.J.; Lewtas, H.J.; Blundell, S.J.; Lancaster, Y.; Franke, I.; Hayes, W.; Pratt, F.L.; Bohatý, L.; Becker, P. Muon-spin relaxation and heat capacity measurements on the magnetoelectric and multiferroic pyroxenes LiFeSi₂O₆ and NaFeSi₂O₆. *Phys. Rev. B* **2010**, *81*, 214403. [\[CrossRef\]](#)
26. Lewtas, H.J.; Lancaster, T.; Baker, P.J.; Blundell, S.J.; Prabhakaran, D.; Pratt, F.L. Local magnetism and magnetoelectric effect in HoMnO₃ studied with muon-spin relaxation. *Phys. Rev. B* **2010**, *81*, 014402. [\[CrossRef\]](#)
27. Oliveira, G.N.P.; Teixeira, R.C.; Moreira, R.P.; Correia, J.G.; Araújo, J.P.; Lopes, A.M.L. Local inhomogeneous state in multiferroic SmCrO₃. *Sci. Rep.* **2020**, *10*, 4686. [\[CrossRef\]](#)

28. Lopes, A.M.L.; Oliveira, G.N.P.; Mendonça, T.M.; Agostinho Moreira, J.; Almeida, A.; Araújo, J.P.; Amaral, V.S.; Correia, J.G. Local distortions in multiferroic AgCrO₂ triangular spin lattice. *Phys. Rev. B* **2011**, *84*, 014434. [CrossRef]
29. Sobolev, A.; Rusakov, V.; Moskvina, A.; Gapochka, A.; Belik, A.; Glazkova, I.; Akulenko, A.; Demazeau, G.; Presniakov, I. ⁵⁷Fe Mössbauer study of unusual magnetic structure of multiferroic 3R-AgFeO₂. *J. Phys. Condens. Matter* **2017**, *29*, 275803. [CrossRef]
30. Sobolev, A.V.; Presnyakov, I.A.; Rusakov, V.S.; Gapochka, A.M.; Glazkova, Y.S.; Matsnev, M.E.; Pankratov, D.A. Mössbauer Study of the Modulated Magnetic Structure of FeVO₄. *J. Exp. Theor. Phys.* **2017**, *124*, 943–956. [CrossRef]
31. Santos, S.S.M.; Marcondes, M.L.; Miranda, I.P.; Rocha-Rodrigues, P.; Assali, L.V.C.; Lopes, A.M.L.; Petrilli, H.M.; Araujo, J.P. Spontaneous electric polarization and electric field gradient in hybrid improper ferroelectrics: Insights and correlations. *J. Mater. Chem. C* **2021**, *9*, 7005–7013. [CrossRef]
32. Dang, T.T.; Schell, J.; Boa, A.G.; Lewin, D.; Marschick, G.; Dubey, A.; Escobar-Castillo, M.; Noll, C.; Beck, R.; Zyabkin, D.; et al. Temperature dependence of the local electromagnetic field at the Fe site in multiferroic bismuth ferrite. *Phys. Rev. B* **2022**, *106*, 054416. [CrossRef]
33. Yeshurun, Y.; Havlin, S.; Schlesinger, Y. Static and dynamic aspects of perturbed angular correlation measurements in perovskite crystals. *Solid State Commun.* **1978**, *27*, 181–184. [CrossRef]
34. Yamada, I. Novel catalytic properties of quadruple perovskites. *Sci. Technol. Adv. Mater.* **2017**, *18*, 541–548. [CrossRef] [PubMed]
35. Presniakov, I.A.; Rusakov, V.S.; Gubaidulina, T.V.; Sobolev, A.V.; Baranov, A.V.; Demazeau, G.; Volkova, O.S.; Cherepanov, V.M.; Goodilin, E.A.; Knot'ko, A.V.; et al. Hyperfine interactions and local environment of ⁵⁷Fe probe atoms in perovskite CaMn₇O₁₂. *Phys. Rev. B* **2007**, *76*, 214407. [CrossRef]
36. Glazkova, Y.S.; Terada, N.; Matsushita, Y.; Katsuya, Y.; Tanaka, M.; Sobolev, A.V.; Presniakov, I.A.; Belik, A.A. High-pressure Synthesis, Crystal Structures, and Properties of CdMn₇O₁₂ and SrMn₇O₁₂ Perovskites. *Inorg. Chem.* **2015**, *54*, 9081–9091. [CrossRef] [PubMed]
37. Belik, A.A.; Glazkova, Y.S.; Katsuya, Y.; Tanaka, M.; Sobolev, A.V.; Presniakov, I.A. Low-Temperature Structural Modulations in CdMn₇O₁₂, CaMn₇O₁₂, SrMn₇O₁₂, and PbMn₇O₁₂ Perovskites Studied by Synchrotron X-ray Powder Diffraction and Mössbauer Spectroscopy. *Phys. Chem. C* **2016**, *120*, 8278–8288. [CrossRef]
38. Dickson, D.P.E.; Berry, F.J. *Mössbauer Spectroscopy*; Cambridge University Press: Cambridge, UK, 1986.
39. Lines, M.E.; Glass, A.M. *Principles and Applications of Ferroelectrics and Related Materials*; Oxford University Press: Oxford, UK, 1977.
40. Strukov, B.A.; Levanyuk, A.P. *Ferroelectric Phenomena in Crystals: Physical Foundations*; Springer: Berlin/Heidelberg, Germany, 1998.
41. Walsh, A.; Payne, D.J.; Egdell, R.G.; Watson, G.W. Stereochemistry of post-transition metal oxides: Revision of the classical lone pair model. *Chem. Soc. Rev.* **2011**, *40*, 4455–4463. [CrossRef]
42. Seshadri, R.; Hill, N.A. Visualizing the Role of Bi 6s “Lone Pairs” in the Off-Center Distortion in Ferromagnetic BiMnO₃. *Chem. Mater.* **2001**, *13*, 2892–2899. [CrossRef]
43. Hussain, S.; Hasanain, S.K.; Jaffari, G.L.; Faridi, S.; Rehman, F.; Abbas, T.A.; Shah, S.I. Size and Lone Pair Effects on the Multiferroic Properties of Bi_{0.75}A_{0.25}FeO_{3-δ} (A = Sr, Pb, and Ba) Ceramics. *J. Amer. Ceram. Soc.* **2013**, *96*, 3141–3148. [CrossRef]
44. Lottermoser, T.; Meier, D. A short history of multiferroics. *Phys. Sci. Rev.* **2020**, *6*, 20200032. [CrossRef]
45. Xia, Z.C.; Xiao, L.X.; Fang, C.H.; Liu, G.; Dong, B.; Liu, D.W.; Chen, L.; Liu, L.; Liu, S.; Doyananda, D.; et al. Effect of 6s lone pair of Bi³⁺ on electrical transport properties of (La_{1-x}Bi_x)_{0.67}Ca_{0.33}MnO₃. *J. Magn. Magn. Mater.* **2006**, *297*, 1–6. [CrossRef]
46. Kaplan, M.D.; Vekhter, B.G. *Cooperative Phenomena in Jahn–Teller Crystals*; Springer: New York, NY, USA, 1995.
47. Alonso, J.A.; Martínez-Lope, M.J.; Casais, M.T.; Fernández-Díaz, M.T. Evolution of the Jahn-Teller Distortion of MnO₆ Octahedra in RMnO₃ Perovskites (R = Pr, Nd, Dy, Tb, Ho, Er, Y): A Neutron Diffraction Study. *Inorg. Chem.* **2000**, *39*, 917–923. [CrossRef] [PubMed]
48. Tachibana, M.; Shimoyama, T.; Kawaji, H.; Atake, T.; Takayama-Muromachi, E. Jahn-Teller distortion and magnetic transitions in perovskite RMnO₃ (R = Ho, Er, Tm, Yb, and Lu). *Phys. Rev. B* **2007**, *75*, 144425. [CrossRef]
49. Johnson, R.D.; Khalyavin, D.D.; Manuel, P.; Radaelli, P.G.; Glazkova, I.S.; Terada, N.; Belik, A.A. Magneto-orbital ordering in the divalent A-site quadruple perovskite manganites AMn₇O₁₂ (A = Sr, Cd and Pb). *Phys. Rev. B* **2017**, *96*, 054448. [CrossRef]
50. Chatterjee, T. Orbital ice and its melting phenomenon. *Indian J. Phys.* **2006**, *80*, 665–675. Available online: <http://hdl.handle.net/10821/211> (accessed on 17 October 2023).
51. Martín-Carrón, L.; de Andrés, A. Melting of the cooperative Jahn-Teller distortion in LaMnO₃ single crystal studied by Raman spectroscopy. *Eur. Phys. J. B* **2001**, *22*, 11–16. [CrossRef]
52. Trokner, A.; Verkhovskii, S.; Gerashenko, A.; Volkova, Z.; Anikeenok, O.; Mikhalev, K.; Eremin, M.; Pinsard-Gaudart, L. Melting of the orbital order in LaMnO₃ probed by NMR. *Phys. Rev. B* **2013**, *87*, 125142. [CrossRef]
53. Schaile, S.; von Nidda, H.-A.K.; Deisenhofer, J.; Eremin, M.V.; Tokura, Y.; Loidl, A. ESR evidence for partial melting of the orbital order in LaMnO₃ below the Jahn-Teller transition. *Phys. Rev. B* **2014**, *90*, 054424. [CrossRef]
54. Ham, F. Jahn-Teller Effects in Mössbauer spectroscopy. *J. Phys. Colloq.* **1974**, *35*, C6-121–C6-130. [CrossRef]
55. Blume, M.; Tjon, J.A. Mössbauer Spectra in a Fluctuating Environment II. Randomly Varying Electric Field Gradients. *Phys. Rev.* **1968**, *165*, 446–456. [CrossRef]
56. Bersuker, I. *The Jahn–Teller Effect*; Cambridge University Press: Cambridge, UK, 2006.
57. Capone, M.; Feinberg, D.; Grilli, M. Crucial role of Jahn-Teller distortions in LaMnO₃. In Proceedings of the Physics in Local Lattice Distortions: Fundamentals and Novel Concepts; Lld2K (Aip Conference Proceedings), Ibaraki, Japan, 23–26 July 2000; American Institute of Physics: New York, NY, USA, 2001; Volume 554, pp. 395–398. [CrossRef]

58. Okamoto, H.; Karppinen, M.; Yamauchi, H.; Fjellvåg, H. High-temperature synchrotron X-ray diffraction study of $\text{LaMn}_7\text{O}_{12}$. *Solid State Sci.* **2009**, *11*, 1211–1215. [[CrossRef](#)]
59. Ghosez, P.; Michenaud, J.-P.; Gonze, X. Dynamical atomic charges: The case of ABO_3 compounds. *Phys. Rev. B* **1998**, *58*, 6224–6240. [[CrossRef](#)]
60. Shannon, R.D.; Fischer, R.X. Empirical electronic polarizabilities in oxides, hydroxides, oxyfluorides, and oxychlorides. *Phys. Rev. B* **2006**, *73*, 235111. [[CrossRef](#)]
61. Wang, C.L.; Li, J.C.; Zhao, M.L.; Zhang, J.L.; Zhong, W.L.; Aragón, C.; Marqués, M.I.; Gonzalo, J.A. Electric field induced phase transition in first order ferroelectrics with large zero point energy. *Phys. A Stat. Mech.* **2008**, *387*, 115–122. [[CrossRef](#)]
62. Wang, C.L.; Qin, Z.K.; Lin, D.L. First-order transition in order-disorder ferroelectrics. *Phys. Rev. B* **1989**, *40*, 680–685. [[CrossRef](#)] [[PubMed](#)]
63. Arnold, D.C.; Knight, K.S.; Morrison, F.D.; Lightfoot, P. Ferroelectric-Paraelectric Transition in BiFeO_3 : Crystal Structure of the Orthorhombic β Phase. *Phys. Rev. Lett.* **2009**, *102*, 027602. [[CrossRef](#)] [[PubMed](#)]
64. Simopoulos, A.; Pissas, M.; Kallias, G.; Devlin, E.; Moutis, N.; Panagiotopoulos, I.; Niarchos, D.; Christides, C. Study of Fe-doped $\text{La}_{1-x}\text{Ca}_x\text{MnO}_3$ ($x \approx 1/3$) using Mössbauer spectroscopy and neutron diffraction. *Phys. Rev. B* **1999**, *59*, 1263–1271. [[CrossRef](#)]
65. Gütlich, P.; Bill, E.; Trautwein, A.X. *Mössbauer Spectroscopy and Transition Metal Chemistry*; Springer: Berlin/Heidelberg, Germany, 2011.
66. Mørup, S.; Madsen, M.B.; Franck, J.; Villadsen, J.; Koch, C.J.W. A new interpretation of Mössbauer spectra of microcrystalline goethite: “Super-ferromagnetism” or “Super-spin-glass” behaviour? *J. Magn. Magn. Mater.* **1983**, *40*, 163–174. [[CrossRef](#)]
67. Bhargava, S.C.; Knudsen, J.E.; Mørup, S. Mössbauer study of spin-spin relaxation of Fe^{3+} ions in the presence of other paramagnetic ions. *J. Phys. Chem. Solids.* **1979**, *40*, 45–53. [[CrossRef](#)]
68. Behr, D.; Belik, A.A.; Khalyavin, D.D.; Johnson, R.D. $\text{BiMn}_7\text{O}_{12}$: Polar antiferromagnetism by inverse exchange striction. *Phys. Rev. B* **2023**, *107*, L140402. [[CrossRef](#)]
69. Jaccarino, V.; Walker, L.R.; Wertheim, G.K. Localized Moments of Manganese Impurities in Ferromagnetic Iron. *Phys. Rev. Lett.* **1964**, *13*, 752–754. [[CrossRef](#)]
70. Brzezicki, W.; Cuoco, M.; Oleś, A.M. Exotic Spin-Orbital Physics in Hybrid Oxides. *J. Supercond. Nov. Magn.* **2017**, *30*, 129–134. [[CrossRef](#)]
71. Brzezicki, W.; Avella, A.; Cuoco, M.; Oleś, A.M. Doped spin-orbital Mott insulators: Orbital dilution versus spin-orbital polarons. *J. Magn. Magn. Mater.* **2022**, *543*, 168616. [[CrossRef](#)]
72. Matsnev, M.E.; Rusakov, V.S. SpectrRelax: An application for Mössbauer spectra modeling and fitting. *AIP Conf. Proc.* **2012**, *1489*, 178–185. [[CrossRef](#)]
73. Sobolev, A.V.; Akulenko, A.A.; Glazkova, I.S.; Belik, A.A.; Furubayashi, T.; Shvanskaya, L.V.; Dimitrova, O.V.; Presniakov, I.A. Magnetic Hyperfine Interactions in the Mixed-Valence Compound $\text{Fe}_7(\text{PO}_4)_6$ from Mössbauer Experiments. *J. Phys. Chem. C.* **2018**, *122*, 19767–19776. [[CrossRef](#)]
74. Stadnik, Z.M. Electric field gradient calculations in rare-earth iron garnets. *J. Phys. Chem. Solids* **1984**, *45*, 311–318. [[CrossRef](#)]
75. Brese, N.E.; O’Keeffe, M. Bond-valence parameters for solids. *Acta Crystallogr. B Struct. Sci. Cryst.* **1991**, *47*, 192–197. [[CrossRef](#)]
76. Khomskii, D.I. *Basic Aspects of the Quantum Theory of Solids*; Cambridge University Press: Cambridge, UK, 2010.
77. Murata, K.K. Directional phase instability on a cubic compressible lattice near a second-order phase transition with a three-component order parameter. *Phys. Rev. B* **1977**, *15*, 4328–4335. [[CrossRef](#)]

Disclaimer/Publisher’s Note: The statements, opinions and data contained in all publications are solely those of the individual author(s) and contributor(s) and not of MDPI and/or the editor(s). MDPI and/or the editor(s) disclaim responsibility for any injury to people or property resulting from any ideas, methods, instructions or products referred to in the content.